The assembly of dusty galaxies at $z \gtrsim 4$: statistical properties

L. Graziani [1,2,3]★ R. Schneider,[1,2,4] M. Ginolfi [5] L. K. Hunt [3] U. Maio,[6]
M. Glatzle[7,8] and B. Ciardi[8]

[1]*Dipartimento di Fisica, Sapienza Università di Roma, Piazzale Aldo Moro 5, I-00185 Rome, Italy*
[2]*INFN, Sezione di Roma I, P.le Aldo Moro 2, I-00185 Rome, Italy*
[3]*INAF/Osservatorio Astrofisico di Arcetri, Largo E. Femi 5, I-50125 Firenze, Italy*
[4]*INAF/Osservatorio Astronomico di Roma, Via di Frascati 33, I-00078 Monte Porzio Catone, Italy*
[5]*Observatoire de Genève, Université de Genève, 51 Ch. des Maillettes, CH-1290 Versoix, Switzerland*
[6]*Leibniz-Institut für Astrophysik, An der Sternwarte 16, D-14482 Potsdam, Germany*
[7]*Physik-Department, Technische Universität München, James-Franck-Straße 1, D-85748 Garching, Germany*
[8]*Max-Planck-Institut für Astrophysik, Karl-Schwarzschild-Straße 1, D-85748 Garching bei München, Germany*

ABSTRACT

The recent discovery of high-redshift dusty galaxies implies a rapid dust enrichment of their
interstellar medium (ISM). To interpret these observations, we run a cosmological simulation
in a $30\,h^{-1}$ cMpc/size volume down to $z \approx 4$. We use the hydrodynamical code DUSTYGADGET,
which accounts for the production of dust by stellar populations and its evolution in the ISM.
We find that the cosmic dust density parameter ($\Omega_{\rm d}$) is mainly driven by stellar dust at $z \gtrsim$
10, so that mass- and metallicity-dependent yields are required to assess the dust content in
the first galaxies. At $z \lesssim 9$, the growth of grains in the ISM of evolved systems [$\log(M_\star/{\rm M}_\odot)$
> 8.5] significantly increases their dust mass, in agreement with observations in the redshift
range $4 \lesssim z < 8$. Our simulation shows that the variety of high-redshift galaxies observed with
the Atacama Large Millimeter Array can naturally be accounted for by modelling the grain
growth time-scale as a function of the physical conditions in the gas cold phase. In addition,
the trends of dust-to-metal and dust-to-gas ($\mathcal{D}$) ratios are compatible with the available data.
A qualitative investigation of the inhomogeneous dust distribution in a representative massive
halo at $z \approx 4$ shows that dust is found from the central galaxy up to the closest satellites along
polluted filaments with $\log(\mathcal{D}) \leq -2.4$, but sharply declines at distances $d \gtrsim 30$ kpc along
many lines of sight, where $\log(\mathcal{D}) \lesssim -4.0$.

Key words: galaxies: evolution – galaxies: formation – cosmology: theory.

1 INTRODUCTION

Recent observations performed with the Atacama Large Millimeter
Array (ALMA)[1] have confirmed the dusty nature of 'normal'
star-forming galaxies[2] at early epochs ($z \geq 4$). Dust continuum
detections (Watson et al. 2015; Knudsen et al. 2017; Laporte et al.
2017), upper limits (Maiolino et al. 2015; Schaerer et al. 2015;
Aravena et al. 2016), and line emissions (Inoue et al. 2016; Bradač
et al. 2017; Olsen et al. 2017) are now available for a limited
sample of these chemically evolved systems (see Casey, Narayanan
& Cooray 2014 for a recent review); however, their number will

certainly increase with future ALMA programmes, with the advent
of the James Webb Space Telescope[3] and with the Extremely Large
Telescope.[4]

To understand the evolution of these galaxies in the epoch
of hydrogen reionization (Behrens et al. 2018) and to interpret
their observables from *ab initio* physical properties (Mancini et al.
2016; Cullen et al. 2017), theoretical models of galaxy formation
accounting for radiative and chemical feedback have been recently
developed (Wise et al. 2012; Graziani et al. 2015, 2017; Xu et al.
2016; Pallottini et al. 2017; Ceverino, Klessen & Glover 2018;
Glatzle, Ciardi & Graziani 2019; Katz et al. 2019). They are of
strategic importance to describe the multiphase, metal-enriched
interstellar medium (ISM) of these early galaxies (Wolfire et al.
2003; Carilli & Walter 2013) and their circumgalactic/intergalactic

★ E-mail: luca.graziani@roma1.infn.it

[1]http://www.almaobservatory.org
[2]In this paper, normal galaxies are identified as non-starburst objects with
star formation rates of a few tens of solar masses per year, representing the
dominant class of galaxies at early cosmic times.

[3]http://www.jwst.nasa.gov/
[4]http://www.eso.org/public/teles-instr/elt/

medium (CGM/IGM) (Finlator et al. 2018). On a cosmological scale, these models can shed light on the impact of cosmic dust on the high-redshift luminosity function (Smit et al. 2016; Koprowski et al. 2017; Ono et al. 2018), on the early stages of cosmic reionization (Eide et al. 2018), and on the colours of galaxy populations (Dunlop et al. 2013).

Over the last few years, improvements have been made in the chemical network of semi-analytical (de Bennassuti et al. 2017; Popping, Somerville & Galametz 2017; Vijayan et al. 2019), seminumerical (Mancini et al. 2015; Khakhaleva-Li & Gnedin 2016; Wilkins et al. 2016; Zhukovska et al. 2016; Ginolfi et al. 2018; Narayanan et al. 2018), and numerical models of galaxy formation (Bekki 2015a,b; Aoyama et al. 2017; McKinnon et al. 2017; Gjergo et al. 2018; Ma et al. 2018), but despite these advancements, the introduction of a comprehensive treatment of cosmic dust in cosmological simulations remains extremely challenging.

The origin and composition of dust grains are highly uncertain and models of dust nucleation in supernova (SN) ejecta (Schneider, Ferrara & Salvaterra 2004; Bianchi & Schneider 2007; Marassi et al. 2015, 2019; Sarangi & Cherchneff 2015; Bocchio et al. 2016; Sluder, Milosavljevic & Montgomery 2018) and in the atmosphere of asymptotic giant branch (AGB) stars (Ferrarotti & Gail 2006; Zhukovska, Gail & Trieloff 2008; Ventura et al. 2012a,b, 2018; Di Crisci, enzo et al. 2013; Nanni et al. 2013, 2014; Dell'Agli et al. 2017, 2019) are required. So far, stellar dust yields adopted in cosmological simulations remain highly unconstrained or model dependent, especially for massive stars with low initial metallicity. In the first galaxies, accurate yields are required to account for the release of metals by the first stars (Pop III; Nozawa et al. 2003; Schneider et al. 2004; Marassi et al. 2014, 2015; Takahashi, Yoshida & Umeda 2018; Chiaki & Wise 2019), and to understand the transition from Pop III to successive generations (Pop II; Maio et al. 2010; Schneider et al. 2012a,b; de Bennassuti et al. 2014; Chiaki et al. 2015). Even the composition of dust in our Galaxy and in its Local Group companions remains a subject of debate, because of uncertainties in interpreting depletion of atomic metals along local lines of sight (Crinklaw, Federman & Joseph 1994; Sofia et al. 2004), the variety of grain chemical compositions, and the difficulties in modelling the observed extinction curves, often contaminated by molecules (Draine 2003; Gordon et al. 2003; Clayton et al. 2015; Ma et al. 2019).

There is observational evidence that dust grains undergo modifications depending on the ISM phase where they reside. Grains can sublimate in extremely hot environments, or can be destroyed by a number of processes such as shattering in grain–grain collisions and thermal sputtering.[5] Shocked gas fronts, propagating in the ISM as a result of SN explosions, are candidate environments in which the above processes act efficiently (Jones et al. 1994; Draine 1995; Caselli, Hartquist & Havnes 1997). Where amorphous dust grains can survive, they significantly evolve by changing their physical properties: mass, size (Hirashita 2012; Roman-Duval et al. 2017), chemical composition (Cecchi-Pestellini et al. 2010), and charge (Weingartner & Draine 2001; Weingartner 2004). These grains can even morph into crystals, if an intense ultraviolet (UV) flux is present (Jones et al. 2013). Depending on the problem at hand and its physical scale and considering the computational cost, numerical implementations generally account for only a subset of the above processes.

Dust production by SNe and AGB stars, as well as processes of grain evolution in the galactic ISM, was implemented in smoothed particle hydrodynamics (SPH) and grid-based schemes (Bekki 2015a,b; Aoyama et al. 2017; McKinnon et al. 2017), while other codes focused on dust feedback in momentum-driven winds (Bekki & Tsujimoto 2014; Hopkins et al. 2014; Hopkins & Lee 2016), or on computing the radiation extinction by radiative transfer through a dusty ISM (Wood & Loeb 2000; Zu et al. 2011; Kimm & Cen 2013; Asano et al. 2014; Hou, Hirashita & Michałowski 2016).

In Mancini et al. (2015), we introduced a novel seminumerical model of dusty galaxies by coupling the results of a semi-analytical code (de Bennassuti et al. 2014) with an SPH simulation (Maio et al. 2010), and we first interpreted the dust mass of normal, high-redshift ($z > 6$) galaxies as a result of production by stars and efficient grain growth in the dense phases of the ISM. The successive coupling with a semi-analytical treatment of radiative feedback allowed us to explain the evolution of galaxy colours (Mancini et al. 2016) and to show that current high-redshift observations already provide important constraints on the nature of dust and its complex evolution in the various phases of the ISM.

Here, we go a step forward by introducing a numerical implementation of our dust model in the cosmological code GADGET (Springel 2005) and successive extensions (Tornatore, Ferrara & Schneider 2007a; Tornatore et al. 2007b; Maio et al. 2009). The new code, named DUSTYGADGET, implements a consistent evolution of grains in different phases of the ISM and follows the spreading of dust and atomic metals by galactic winds throughout the scales of CGM and IGM.

The paper is organized as follows. In Section 2, we describe the numerical implementation of our code, while the set-up of the galaxy formation simulation is provided in Section 3. Section 4 introduces the theoretical models used to benchmark the findings of Section 3. Finally, the simulation results are provided in Section 5: the redshift evolution of the dust content is described in Section 5.1 and the statistics of our galaxy sample are discussed in Section 5.2 and carefully compared to current observations at $z \geq 4$. A qualitative analysis of the spatial distribution of dust in a massive dusty halo at $z \approx 4$ is the subject of Section 5.3. The results of our investigation are summarized and discussed in Section 6.

2 DUSTYGADGET

Here, we describe the main features of DUSTYGADGET and their numerical implementation. Section 2.1 and Appendix A summarize the chemical network and the ISM model inherited from previous implementations, while Sections 2.2 and 2.3 focus on dust production by stars and the evolution of grains in the multiphase ISM.

2.1 Chemical network: atomic metals and molecules

DUSTYGADGET derives its gas chemical evolution model from the original implementation of Tornatore et al. (2007b). The model relaxes the so-called instantaneous recycling approximation and follows the metal release from stars of different masses, metallicity, and lifetimes (Padovani & Matteucci 1993). Different models of the adopted metal yields, as well as alternative initial mass functions (IMFs) or functional forms of the adopted stellar lifetime, can also be easily implemented in the code and their impact on the results explored (Romano et al. 2005, 2010; Vincenzo et al. 2016). Mass- and metallicity-dependent yields are implemented for Pop II/I stars: for low- and intermediate-mass stars, we adopt van den Hoek & Groenewegen (1997), while results from Woosley & Weaver (1995)

---

[5]The interested reader is referred to Draine (2011) and references therein.

are included to describe core-collapse SNe. Finally, for Type Ia SNe (SNeIa) we use Thielemann et al. (2003). Stars with masses $\geq 40 \, M_\odot$ are assumed to collapse into black holes and do not contribute to metal enrichment. Pop III stars with masses in the range [140, 260] $M_\odot$ are expected to explode as pair-instability SNe (PISNe) and their mass-dependent yields are taken from Heger & Woosley (2002). Outside this range, they are assumed to directly collapse into black holes. The chemical network present in DUSTYGADGET also includes the evolution of both atomic and ionized hydrogen, helium, and deuterium, as described in Yoshida et al. (2003), Tornatore et al. (2007b), and Maio et al. (2010). Reactions leading to the creation or destruction of primordial molecules are also included following Maio et al. (2007) and the gas cooling function consistently reflects the chemical network by accounting for molecular, atomic, and fine structure metal transitions of O, C^+, Si^+, and Fe^+ at $T < 10^4$ K (Sutherland & Dopita 1993; Yoshida et al. 2003; Maio et al. 2007; Wiersma, Schaye & Smith 2009).

2.2 Dust production by stars

Dust production by stars is implemented to ensure consistency with gas-phase metal enrichment: mass- and metallicity-dependent dust yields, consistent with the ones described in Section 2.1, are computed for different stellar populations. Hence, in this first implementation of DUSTYGADGET, dust yields for Pop III PISNe are taken from Schneider et al. (2004), which in turn have been computed from the grid of PISN models by Heger & Woosley (2002). For Pop II/I core-collapse SNe, we use the yields from Bianchi & Schneider (2007) (based on the SN models by Woosley & Weaver 1995), while for AGB stars we adopt the yields from Ferrarotti & Gail (2006) and Zhukovska et al. (2008) (derived from the models of van den Hoek & Groenewegen 1997). However, alternative sets of consistent metal and dust yields could be adopted in future works to explore the impact of more recent calculations of core-collapse SNe (Marassi et al. 2019) and AGB dust yields (Ventura et al. 2012b, a, 2018; Di Criscienzo et al. 2013; Dell'Agli et al. 2017, 2019). It would be possible to also explore the impact of different mass ranges and slopes of the Pop III IMF that are still poorly constrained by numerical simulations (Hirano et al. 2014, 2015) and stellar archaeology studies (de Bennassuti et al. 2017).

An important aspect that has to be considered when evaluating SN dust yields is the effect of the reverse shock (RS) on the mass of dust nucleated in the SN ejecta (Bianchi & Schneider 2007; Nozawa et al. 2007; Silvia, Smith & Shull 2010, 2012; Marassi et al. 2015; Bocchio et al. 2016; Micelotta, Dwek & Slavin 2016). The concerted impact of thermal and non-thermal sputtering by collisions with energetic gas particles in shocked regions can lead to the erosion of dust grains on time-scales of $\sim 10^5$ yr. Depending on the density of the circumstellar medium (typically $\rho_{ISM} = 10^{-25}$ to 10^{-23} g cm^{-3}), Bianchi & Schneider (2007) find that only a fraction of the dust mass (from 2 to 20 per cent) survives the passage of the RS. This is a significant reduction that cannot be neglected when estimating the contribution of SNe to interstellar dust enrichment. In a more recent study, Bocchio et al. (2016) compare the dust masses inferred from observations of four well-studied SN remnants in the Milky Way and Magellanic Clouds (SN 1987A, CasA, the Crab Nebula, and N49) by adopting theoretical models that self-consistently follow the dynamics of the grains and account for the effects of the forward and reverse shocks. For all the simulated models, they predict the time evolution of the dust mass in the shocked and unshocked regions of the ejecta and find good agreement with the values estimated from observations (see

their fig. 4). However, since the oldest SN has an estimated age of 4800 yr and the largest dust mass destruction is predicted to occur between 10^3 and 10^5 yr after the explosions, current observations can only provide an upper limit on the average/effective dust yield of about $(1.55 \pm 1.48) \times 10^{-2} \, M_\odot$; this is in good agreement with the estimates of Bianchi & Schneider (2007) for a moderate destruction efficiency (or, equivalently, a circumstellar medium density of $\rho_{ISM} = 10^{-24}$ g cm^{-3}). As the RS acts on spatial and temporal scales smaller than the cosmological ones, its impact is accounted for by an *effective* dust yield, as described in the above models.

The tables of stellar dust yields adopted in DUSTYGADGET are in agreement with findings by previous studies (Valiante et al. 2009, 2011, 2014; de Bennassuti et al. 2014) allowing us to safely compare numerical results across different modelling strategies and over samples of galaxies at high (Mancini et al. 2015, 2016) and low (Ginolfi et al. 2018) redshifts. Although yields describing the mass and size distribution of individual dust species are available, in the current implementation four classes are accounted for: carbon, silicates ($MgSiO_3$, Mg_2SiO_4, and SiO_2), alumina (Al_2O_3), and iron (Fe) dust grains. Our chemical evolution model is, however, sufficiently flexible to include other grain types and to explore combinations of stellar yields and different assumptions on the shapes of the stellar IMF. This is particularly important when dealing with the first phases of dust enrichment operated by Pop III SN explosions as the shape of the IMF and the properties of these events are still very uncertain (de Bennassuti et al. 2017).

As a final remark, we point out that DUSTYGADGET does not explicitly follow the evolution of the grain size distribution once the grains enter the ISM. An explicit computation has been shown to be very expensive (Asano et al. 2013b; McKinnon et al. 2018), while a simplified treatment based on a two-size approximation (Hirashita 2015) can easily reproduce the main features when implemented in hydrodynamical simulations (Aoyama et al. 2017). We plan to include the above approximation in a future work.

2.3 Dust evolution in the ISM

Once the grains produced by stars are released into the ISM, depending on the environment, they experience a number of physical processes altering their chemical composition, size, charge, and temperature. While dust-to-light interactions (e.g. photoheating, grain charging) do not change the mass of dust unless the grain temperature reaches the sublimation threshold (typically $T_{d,s} \gtrsim 10^3$ K), other mechanical (i.e. sputtering) and chemical feedback (i.e. grain growth) can alter both the total mass and grain size distribution (Draine 2003, 2011).[6] A complete dust model should provide a self-consistent evolution of both total dust mass and grain properties (size and temperature at least; see the thorough review by Hirashita 2013). In this first study, we do not follow the evolution of grain sizes but only consider the physical processes that directly alter the dust mass: astration, grain growth, destruction by interstellar shocks, and grain sputtering in the hot ISM phase.

Our implementation relies on the widely adopted multiphase ISM model introduced by Springel & Hernquist (2003) in GADGET2. Appendix A summarizes its features, while the interested reader can find more details in the original paper.

---

[6]In addition, some other mass conserving processes, such as grain coagulation and shattering (i.e. fragmentation by grain–grain collisions), can have profound implications on the grain size distribution.

DUSTYGADGET accounts for dust evolution by implementing the diffuse and condensed phases of our semi-analytical models (de Bennassuti et al. 2014; Mancini et al. 2015, 2016) on top of the hydrodynamical ISM scheme. In each star-forming SPH particle, a two-phase ISM is assumed to structure in hot and cold phases, which are equivalent to the diffuse and condensed phases mentioned earlier. In this way, at each time-step dt, equations (7) and (8) of Mancini et al. (2016) simply apply, by adapting the nomenclature 'diff' $\rightarrow_h$ and 'MC' $\rightarrow_c$:

$$\dot{M}_{d,c} = \dot{M}_c^{\mathcal{D}}(t) - SFR(t)\,\mathcal{D}_c + \frac{M_{d,c}(t)}{\tau_{gg}},$$

$$\dot{M}_{d,h} = -\dot{M}_c^{\mathcal{D}}(t) + \dot{Y}_d(t) - \frac{M_{d,h}(t)}{\tau_d}, \tag{1}$$

where $SFR(t)$ is the time-dependent star formation rate and $\mathcal{D} = M_d/M_g$ is the particle mass fraction in dust. τ_d and τ_{gg} are the dust destruction and accretion time-scales, respectively, and $\dot{M}_c^{\mathcal{D}}$ describes the dust mass exchange between the hot phase and the cold phase. Finally, $\dot{Y}_d$ is the dust yield produced by the stellar sources and it depends on the SFR, the IMF, and the adopted type of metal and dust yields of the specific simulation run (see discussion in Section 2.2). First, in a numerical scheme featuring an explicit multiphase model, the exchange term $\dot{M}_c^{\mathcal{D}}$ can be directly derived from the mass present in each phase as established by equation (A2). Secondly, the gas-to-dust ratio $\mathcal{D}_c$ is computed through the cold gas fraction (x_c). With the above nomenclature, the evolution of the dust mass in each SPH gas particle becomes

$$\dot{M}_d = -SFR(t)\,\mathcal{D}_c + \frac{x_c M_d}{\tau_{gg}} - (1-x_c)M_d\left(\frac{1}{\tau_d} + \frac{3}{\tau_{sp}}\right) + \dot{Y}_d(t). \tag{2}$$

The interpretation of this equation is straightforward: during a time-step dt, each star-forming SPH particle evolves by losing dust mass through astration (SFR $\mathcal{D}_c$), grain destruction [$(1-x_c)M_d/\tau_d$], and sputtering [$(1-x_c)M_d/\tau_{sp}$]; at the same time, it gains mass by stellar evolution ($\dot{Y}_d$) and grain growth ($x_c M_d/\tau_{gg}$). Note that in this final expression we explicitly added a sputtering term (with typical time-scale τ_{sp}) to the destruction processes, and it applies to all dust-contaminated particles present in the hot gas phase (also see details of equation 7).

Here, we recap how the dust mass of a single star-forming gas particle is evolved in each time-step dt. First, the cold fraction from the previous iteration is used to grow the dust mass in the metal-enriched cold gas on the time-scale τ_{gg}. Secondly, as the gas cools down and forms stars, the astration term traps dust into newly formed stellar particles. Finally, SN enrichment injects new grains in the hot phase (the dust mass is accounted for by stellar yields described in Section 2.2) while shocks destroy them in the time-scale τ_d. Note that in the hot phase the sputtering term erodes grains on time-scale τ_{sp}.

By iterating this process consistently with the chemical scheme, the mass of the various dust species evolves in time in SPH particles.

2.3.1 Grain destruction by shocks

Dust grains can be destroyed by sputtering or shattering in hot ISM regions running over SN shocks. The dust destruction time-scale τ_d is modelled as

$$\tau_d = \frac{M_h}{R'_{SN}\epsilon_d M_s(v_s)} \tag{3}$$

(Valiante et al. 2011; de Bennassuti et al. 2014), where for core-collapse SNe

$$M_s(v_s) = \frac{\langle E_{51}\rangle}{\langle v_{SN}^2\rangle} = 6800\,M_\odot\,\langle E_{51}\rangle/(v_{SN}/(100\,km\,s^{-1})^2 \tag{4}$$

is the mass shocked up to a velocity of at least v_{SN} by an SN in the Sedov–Taylor phase. By adopting $\langle v_{SN}\rangle \sim 200\,km\,s^{-1}$ and $\langle E_{51}\rangle \approx 1.2$ as the average SN energy in units of 10^{51} erg, we obtain a typical value of $M_s(v_s) \approx 2040\,M_\odot$.

R'_{SN} is the *effective* SN rate, since not all SNe are equally efficient at destroying dust (McKee 1989); it is defined by scaling the total SN rate (R_{SN}) of the gas particle with a suitable factor f_{SN}: $R'_{SN} = f_{SN}R_{SN} \approx 0.15R_{SN}$. Finally, the value assumed for the dust destruction efficiency is $\epsilon_d = 0.48$ (Nozawa, Kozasa & Habe 2006).

For PISN we adopt, in the same equations, $\epsilon_d = 0.60$, $f_{PISN} = 1$, $\langle E_{51}\rangle \approx 27$, and then $M_s(v_s) \approx 4.59 \times 10^4\,M_\odot$. The resulting grain destruction time-scales are then

$$\tau_{d,SN} = 6.8 \times 10^3 \left(\frac{M_h}{10^6\,M_\odot}\right)\left(\frac{1}{R_{SN}}\right),$$

$$\tau_{d,PISN} = 36.3 \left(\frac{M_h}{10^6\,M_\odot}\right)\left(\frac{1}{R_{PISN}}\right). \tag{5}$$

The numerical implementation of these formulae is straightforward in SPH: each time a gas particle is evaluated for stellar evolution, the types of exploding SNe are accounted for, their rates derived, and the mass in hot phase computed after explosion.[7]

2.3.2 Grain growth

In the cold ISM phase, dust can grow in mass by sticking atomic metals on to grain surfaces. While the atomic process is not fully understood from its chemical principles and strictly depends on both environment properties and grain chemical composition and sizes (Ceccarelli et al. 2018), a commonly adopted parametrization of the grain growth time-scale $\tau_{gg}(n_c, T_c, Z_c)$ is

$$\tau_{gg} = 2.0\,Myr \times \left(\frac{n_c}{1000\,cm^{-3}}\right)^{-1}\left(\frac{T_c}{50\,K}\right)^{-1/2}\left(\frac{Z_c}{Z_\odot}\right)^{-1}$$

$$= \tau_{gg,0}(n_c, T_c)\left(\frac{Z_c}{Z_\odot}\right)^{-1}, \tag{6}$$

where grains are assumed spherical with a typical size of ≈ 0.1 μm (Hirashita et al. 2014), and n_c and T_c are the number density and temperature of the cold gas phase, respectively. Z_c is the gas metallicity computed by the total mass of atomic metals in the gas phase.

For gas at solar metallicity with $n_c = 10^3\,cm^{-3}$ and $T_c = 50\,K$, the accretion time-scale becomes $\tau_{gg,0} = 2.0\,Myr$ (see Asano et al. 2013b). de Bennassuti et al. (2014) show that this value reproduces the observed dust-to-gas ratio of local galaxies over a wide range of gas metallicity; it also provides predictions consistent with the upper limits inferred from deep ALMA and PdB observations of galaxies at $z > 6$ (Mancini et al. 2015).

DUSTYGADGET computes τ_{gg} in the cold phase of star-forming particles by relying on the physical conditions in the model, unlike the usual schemes that assume fixed values for n_c and T_c (see e.g.

---

[7]It should be noted that in cosmological simulations the propagating environment of SN shocks is likely represented by the same SPH particle, while in zoom-in simulations a criterion to define the affected environment must be adopted, as explained in Aoyama et al. (2017).

Mancini et al. 2015, 2016). Z_c is consistently computed from the mass of atomic metals and gas available in the model. In agreement with the ISM scheme (see Appendix A), we compute n_c by assuming that it is entirely composed of a neutral atomic gas mixture of hydrogen and helium with a mean molecular weight $\mu = 1.22$ (Barkana & Loeb 2001). In reality, the cold ISM phase observed in galaxies comprises both atomic and molecular regions and a more realistic model should rely on a consistent implementation of both the H_2 formation process on dust grains and its photodissociation under a Lyman–Werner flux. We defer the treatment of these additional mechanisms to a future study, also linking star formation to H_2, rather than total cold gas including HI.

We also note that in equation (6) the value of the scaling factor $\tau_{gg,0}$ depends on the evolution of T_c. As summarized in Appendix A and detailed in Springel & Hernquist (2003), the multiphase implementation of the ISM does not explicitly follow the evolution of T_c but only assumes a fiducial, average value of $T_c = 10^3$ K, i.e. a constant energy per unit mass of the cold gas (u_c). While the evolution of the hot phase is proven not to depend strongly on this assumption (see references in Appendix A), grain growth becomes efficient at cooler ambient temperatures (i.e. $T_c \approx 50$–100 K), but an astrophysical characterization of this environment is still unknown. Ceccarelli et al. (2018) have shown that in cold molecular clouds ($n \approx 1000$ cm^{-3}, $T \approx 10$–20 K) dust grains can easily develop icy mantles so that their growth has a problematic chemical justification. In the cold neutral medium ($n \approx 30$ cm^{-3}, $T \approx 100$ K), grains can probably grow, particularly if Coulomb focusing enhances the collision rate, as suggested by Weingartner & Draine (1999) and Zhukovska, Henning & Dobbs (2018). Hereafter, as a compromise, a value of $T_c = 50$ K is adopted in our model.

As for the destruction term described in Section 2.3.1, the numerical implementation of the grain growth process is straightforward in our SPH scheme: at each time-step, we compute the fraction of cold mass of star-forming SPH particles, account for the dust mass in the cold phase, and finally increase it by the growth term.

2.3.3 Grain sputtering

Once the grains enter a hot plasma ($T_h \gtrsim 10^6$ K), they are sputtered away by thermal collisions with both protons and helium nuclei. This process has been modelled in the past by many authors (Draine & Salpeter 1979a,b; Seab 1987; Tielens et al. 1994) and included in models of dust evolution in elliptical galaxies, where the hot phase largely dominates the galactic ISM (Tsai & Mathews 1995). The sputtering time-scale τ_{sp} on spherically modelled grains depends on the plasma number density n_h, the temperature T_h, and the grain size $a(t)$. In the above models, it is defined as inversely proportional to the rate at which a decreases in time, i.e.

$$\tau_{sp} = a \left| \frac{da}{dt} \right|^{-1},$$

$$\left| \frac{da}{dt} \right| = -3.2 \times 10^{-18} \text{ cm}^4 \text{ s}^{-1} \left(\frac{\rho}{m_p} \right) \left[\left(\frac{2 \times 10^6 \text{ K}}{T_h} \right)^{2.5} + 1 \right]^{-1},$$

where ρ and m_p are the gas density and proton mass, respectively. Also note that this approximation is valid for both silicate and carbon dust. Coherently with the grain growth assumptions and the temperature of the hot phase of SPH particles, here we adopt an explicit expression for τ_{sp} by assuming spherical grains with typical size of $a \approx 0.1$ µm and collisional ionization of the gas. This leads

to the formula

$$\tau_{sp} = 1.68 \times 10^{-4} \text{ Gyr} \left(\frac{n_h}{\text{cm}^{-3}} \right)^{-1} \left[\left(\frac{2 \times 10^6}{T_h} \right)^{2.5} + 1 \right]. \quad (7)$$

In this way, the sputtering term in equation (2) becomes $-M_d/(\tau_{sp}/3)$. Finally note that for temperatures $T_h < 10^6$ K, sputtering becomes very inefficient and dust grains could easily survive in a diffuse, photoionized IGM once spread by galactic winds.

2.4 Spreading of atomic metals and dust by galactic winds

In its first implementation, DUSTYGADGET adopts the wind prescription implemented in Springel & Hernquist (2003), on top of which metals are spread in the surrounding gas as described by Tornatore et al. (2007b). At the end of stellar evolution, metals and dust are then distributed in the surroundings of a star-forming region by using a spline-type kernel of the SPH scheme and by weighting over 64 neighbours according to the influence region of each particle. The dust distribution simply follows the atomic metal spreading without accounting for any momentum transfer through dust grains (see McKinnon et al. 2018 for a recent implementation that accounts for dynamical forces acting on dust particles). At the same time, dusty particles associated with galactic winds evolve in their hot phase through sputtering. As a result, the dust-to-metal ratio will be modulated depending on the environment, attaining different values for the galactic ISM, CGM, and IGM.

3 GALAXY FORMATION SIMULATION

The features of DUSTYGADGET have been exploited in a new hydrodynamical simulation performed on a periodic, co-moving box size of $30 \, h^{-1}$ cMpc, and assuming a lambda cold dark matter cosmology consistent with WMAP7 data release (Komatsu et al. 2011).[8] The simulation starts from a neutral gas configuration at $z = 100$ and zero metallicity, and evolves $\approx 320^3$ particles per gas and dark matter (DM) species with masses of 9×10^6 and $6 \times 10^7 \, h^{-1} \, M_\odot$, respectively, down to $z = 4$; 30 outputs at intermediate redshifts are stored during the run. For a better comparison with Mancini et al. (2015), we adopted a chemical set-up close to the one described in Maio et al. (2010) including molecules and atomic metals, while simulating a larger cosmic volume to match the galaxy sample in Mancini et al. (2016). Hereafter, we briefly summarize the relevant properties of the run. Stars are formed from the cold gas phase once the density exceeds a threshold value of $n_{th} = 132 \, h^{-2} \, \text{cm}^{-3}$ (physical); this choice allows the capture of all the relevant phases of cooling until the onset of runaway collapse (Maio et al. 2009). As in Tornatore et al. (2007a), stellar populations follow an IMF consistent with the metallicity of stellar particles ($Z_\star$) and the transition from Pop III to Pop II stars is modelled by assuming that metal fine structure cooling is efficient at a gas critical metallicity $Z_{cr} = 10^{-4} \, Z_\odot$ (Maio et al. 2007). Below Z_{cr}, the IMF is assumed to follow a Salpeter power-law slope in the mass range [100, 500] $M_\odot$, while above Z_{cr} a standard Salpeter IMF in the mass range [0.1, 100] $M_\odot$ is adopted. An extensive investigation on the impact of the adopted Pop III IMF and Z_{cr} on the earliest phases of star formation and chemical enrichment would require a higher mass resolution that can be achieved only by

---

[8] $H_0 = 100 \, h \, \text{km s}^{-1} \, \text{Mpc}^{-1}$ with $h = 0.7$, $\Omega_{m,0} = 0.3$, $\Omega_{b,0} = 0.04$, $\Omega_{\Lambda,0} = 0.7$, $\Omega_{tot,0} = 1.0$, and $\sigma_8 = 0.9$.

Table 1. Summary of theoretical models adopted for a comparison with DUSTYGADGET. References for ISM models: (*a*) Springel & Hernquist (2003), Maio et al. (2010); (*b*) Arrigoni et al. (2010), Somerville, Popping & Trager (2015); (*c*) Gioannini, Matteucci & Calura (2017b), Gioannini et al. (2017a); (*d*) Aoyama et al. (2017); (*e*) Vogelsberger et al. (2013). References for stellar dust yields and dust growth models: (*f*) Dwek (1998, 2016); (*g*) Zhukovska et al. (2008); (*h*) Piovan et al. (2011); (*i*) Bianchi & Schneider (2007); (*l*) Inoue (2011a,b), Kuo & Hirashita (2012); (*m*) Marassi et al. (2019); (*n*) Dell'Agli et al. (2017); (*o*) Bocchio et al. (2016); (*p*) Hirashita et al. (2014); (*q*) Zhukovska (2014); (*u*) Saitoh (2017); (*v*) Slavin, Dwek & Jones (2015); (*z*) Hirashita (2000). Reference for grain sputtering: (*r*) Tsai & Mathews (1995). References for grain destruction: (*s*) McKee (1989); (*t*) Asano et al. (2013b).

Name	Type	Simulation	ISM	Yields	Accretion	Thermal sputtering	Destruction
Popping+17	Semi-analytical	'Fiducial'	*b*	*f*	*q, f*	*r*	*v*
Mancini+15	Semi-numerical	'SN + AGB + GG'	*a*	*g, i*	*p*	−	*s*
Gioannini+17	Analytical	'Alternative'	*c*	*h*	*z, t*	−	*t*
Aoyama+18	SPH-GADGET3-OSAKA	'L50n512'	*d*	*l, u*	*p*	*r*	*s*
McKinnon+17	MovingMesh-AREPO	'L25n512'	*e*	*f*	*f*	*r*	*s*
DUSTYGADGET	SPH-GADGET2	'RefRun'	*a*	*g, i, m, n, o*	*p*	*r*	*s*

simulating smaller cosmological volumes (Xu et al. 2016). We will defer this point to a future study where an approximate treatment of radiative feedback will be also implemented in our model (Maio et al. 2016).

Galactic-scale winds associated with star-forming regions are assumed with a constant velocity of 500 km s^{-1}, in line with recent estimates of star-formation-driven outflows in normal galaxies at $z > 4$ (Sugahara et al. 2019; Ginolfi et al. 2020). Finally, radiative feedback is implemented by adopting a cosmic UV background (Haardt & Madau 1996) and accounting for photoionization, which affects gas cooling and hence star formation. Although this chemical evolution model can be extended to track a large number of metal species, in the current simulation we restrict the analysis to the following atomic metals: C, O, Mg, S, Si, and Fe.

DM haloes and their substructures are found by running the halo finder code AMIGA (Gill, Knebe & Gibson 2004; Knollmann & Knebe 2009) and the catalogue has been verified to be consistent with the friends-of-friends and SUBFIND implemented in GADGET (Springel et al. 2001) and adopted in Mancini et al. (2016). Galaxies are identified as bound groups of at least 32 total (DM + gas + star) particles; only galaxies containing at least 10 stellar particles are considered.

4 REFERENCE THEORETICAL MODELS AND OBSERVATIONS

To assess the reliability of our results, DUSTYGADGET is compared with a series of analytical, semi-analytical, and numerical schemes. We selected the study of Gioannini et al. (2017b), which combines a series of analytical prescriptions to evolve the number density of a pre-assigned class of galaxy morphologies, and the semi-analytical model of Popping et al. (2017); both models include processes of dust formation and evolution. Our previous study, introduced in Mancini et al. (2015), is added as a semi-numerical model and complemented with two reference hydrodynamical schemes: a moving mesh-based implementation in AREPO (McKinnon et al. 2017) and an SPH, GADGET-based code (Aoyama et al. 2018).

Table 1 summarizes the literature references with the algorithm type, the ISM model, the implementation of dust yields, and the physics of dust evolution: grain growth and destruction.[9] Additional details and a summary of their efficiency parameters are provided in Appendix B.

The production of dust by stellar sources relies on different yields and physical assumptions: recent models implement mass- and metallicity-dependent tabulated values and account for the partial destruction of SN dust by the RS (Mancini et al. 2015; DUSTYGADGET), while other implementations still rely on extrapolated trends, including the RS effects through an average correction (e.g. Popping et al. 2017). A disagreement on the sources of dust production is also present: Popping et al. (2017), McKinnon et al. (2017), and Aoyama et al. (2018) assume that SNeIa can produce dust, while the remaining models are more conservative and exclude these SNe as dust producers. Finally, DUSTYGADGET is the only code that explicitly accounts for the contribution of PISNe at the highest redshifts (see Section 2.2 for more details).

The implementation of dust evolution requires a two-phase description of the galactic ISM in all approaches, by assuming a certain cold fraction x_c (Mancini et al. 2015; Gioannini et al. 2017b; McKinnon et al. 2017; Aoyama et al. 2018), by consistently taking it from star-forming particles (DUSTYGADGET), or by deriving it from an explicit description of the H_2 molecular phase (Popping et al. 2017). Differences also exist in the implementation of the accretion and destruction mechanisms and in the adopted time-scales. Table B1 shows that $\tau_{gg,0}$ varies in the 1.2–4.0 Myr range across models, while the value of the swept mass and destruction efficiencies are tuned either by assuming different reference values for the shock speed or by correcting the SN rates across SN types (see the values of f_{SN}, ϵ_d, and M_s in Table B1). Finally note that only Popping et al. (2017) distinguish between carbonaceous- and silicon-based dust when destroying the grains, while Aoyama et al. (2018) is the only model that considers a grain size distribution.

The implementation of dust sputtering, when present, is consistent across models and relies on the description of Tsai & Mathews (1995).

To compare the predictions of our simulation with observations available at $z \geq 4$, we collected a sample of dusty galaxies in the redshift range $3.5 < z < 9.5$. Table 2 summarizes their physical properties: redshift (z), log($M_\star$), SFR [derived from the UV or the infrared (IR) flux], log(M_d), and the dust temperature T_d.[10] The last two values are either inferred by dust continuum detections or derived as in Schaerer et al. (2015) and Mancini et al. (2015). Galaxies are also grouped in redshift bins of $\Delta z = 1$, centred at $z = 9, 8, 7, 6, 5$, and 4, and are selected in the stellar mass range covered

---

[9]Other important processes, e.g. the coagulation of dust grains, have not been considered because they do not change the total mass of dust.

[10]Note that when the dust mass depends on different assumptions for T_d, the values of temperature and mass are listed in the same order.

Table 2. Physical properties of the galaxy sample in Fig. 3 collected from the literature: galaxy redshift z, logarithm of the stellar mass $M_\star$, star formation rate (when available the values derived from the UV and IR components are indicated), logarithm of the dust mass M_d, and dust temperature. When the dust mass is derived from scaling relations by assuming a value of T_d, the corresponding values are listed in the same order in both columns. References: (a) Laporte et al. (2017); (b) Tamura et al. (2019); (c) Schaerer et al. (2015); (d) Knudsen et al. (2017); (e) Hashimoto et al. (2019); (f) Maiolino et al. (2015), Mancini et al. (2015); (g) Iye et al. (2006); (h) da Cunha et al. (2015); (i) Capak et al. (2015), Mancini et al. (2016), Faisst et al. (2017); (l) Cooray et al. (2014); (m) Strandet et al. (2017), Marrone et al. (2018); (n) Dessauges-Zavadsky et al. (2017); (o) Bakx et al. (2020).

Name	z	$\log(M_\star)$ $(M_\odot)$	SFR (UV; IR) $(M_\odot\,\mathrm{yr}^{-1})$	$\log(M_d)$ $(M_\odot)$	T_d (K)
A2744_YD4[a]	8.382	$9.29^{+0.25}_{-0.17}$	$20^{+17.6}_{-9.5}$	$6.74^{+0.66}_{-0.16}$	37–63
MACS0416_Y1[b]	8.312	$8.38^{+0.11}_{-0.02}$	$55^{+175}_{-0.2}$	$6.91^{+0.07}_{-0.09}$; $6.56^{+0.07}_{-0.1}$	40; 50
MACS0416_Y1[o]	8.312	$8.38^{+0.11}_{-0.02}$	–	6.23; 5.76	50; 90
z8-GND-5296[c]	7.508	9.7 ± 0.3	23.4; <113	<8.69; <8.13; <7.81	25; 35; 45
A1689-zD1[d]	7.500	9.4 ± 0.1	$14.0^{+8.0}_{-8.0}$	7.2 ± 0.2	40.5
B14-65666[e]	7.170	$8.89^{+0.01}_{-0.04}$	200^{+82}_{-39}	$7.05^{+0.04}_{-0.09}$; $6.97^{+0.03}_{-0.09}$; $6.91^{+0.08}_{-0.1}$	48; 54; 61
BDF-3299[f]	7.109	9.30 ± 0.30	5.7; –	<7.32; <6.50	27.6; 45
BDF-512[f]	7.008	9.30 ± 0.30	6.0; –	<7.72; <6.89	27.6; 45
IOK-1[g]	6.960	9.70 ± 0.30	20.4; <16.3	< 7.84; < 7.29; <6.98	25; 35; 45
SPT0311−58E[m]	6.900	$10.54^{+0.15}_{-0.24}$	13.0; $<540 \pm 175$	$8.60^{+0.18}_{-0.30}$	36–115
SDF-46975[f]	6.844	9.80 ± 0.30	15.4; –	<7.76; <6.94	27.6; 45
A1703-zD1[g]	6.800	9.20 ± 0.30	9.0; 13.8	<7.76; <7.22; <6.91	25; 35; 45
Himiko[g]	6.595	9.80 ± 0.30	32.3; 11.4	<7.67; <7.13; <6.83	25; 35; 45
HCM 6A[g]	6.560	9.50 ± 0.30	13.7; 24.5	<8.0; <7.47; <7.17	25; 35; 45
HFLS 3[l]	6.34	10.70	–; 1320	8.48	24–50
ALESS061.1[h]	6.120	$10.59^{+0.02}_{-0.25}$	$1380.38^{+525.08}_{-690.55}$	$8.579^{+0.62}_{-0.22}$	$57.0^{+0.62}_{-0.22}$
ALESS072.1[h]	5.820	$10.95^{+0.14}_{-0.41}$	$549.54^{+863.00}_{-414.64}$	$8.930^{+0.61}_{-0.14}$	44.0^{+18}_{-14}
HZ1[i]	5.690	10.00 ± 0.30	31.7; –	<7.93; <7.42; <7.13	25; 35; 45
HZ2[i]	5.670	10.00 ± 0.30	32.4; –	<7.91; <7.40; <7.11	25; 35; 45
HZ10[i]	5.660	10.30 ± 0.30	50.12; –	<9.07; <8.56; <8.27	25; 35; 45
HZ3[i]	5.550	9.89 ± 0.30	23.5; –	<8.14; <7.64; <7.34	25; 35; 45
HZ9[i]	5.550	9.79 ± 0.30	23.5; –	<8.66; <8.16; <7.87	25; 35; 45
ALESS065.1[h]	5.680	$10.74^{+0.17}_{-0.48}$	$436.51^{+765.75}_{-321.69}$	$8.910^{+0.56}_{-0.48}$	44.0^{+17}_{-16}
HZ4[i]	5.540	10.20 ± 0.30	40.8; –	<8.25; <7.75; <7.46	25; 35; 45
HZ5[i]	5.300	10.40 ± 0.30	64.7; –	<7.90; <7.40; <7.11	25; 35; 45
HZ6[i]	5.290	10.20 ± 0.30	48.0; –	<8.02; <7.52; <7.23	25; 35; 45
HZ7[i]	5.250	9.96 ± 0.30	27.0; –	<7.94; <7.44; <7.15	25; 35; 45
ALESS001.2[h]	5.220	$10.90^{+0.13}_{-0.39}$	$416.87^{+758.03}_{-339.24}$	$8.69^{+0.61}_{-0.37}$	45.0^{+21}_{-16}
HZ8[i]	5.140	9.89 ± 0.30	23.5; –	<7.84; <7.34; <7.06	25; 35; 45
ALESS001.1[h]	4.780	$10.97^{+0.15}_{-0.42}$	$602.56^{+1259.53}_{-432.74}$	$9.12^{+0.49}_{-0.46}$	42.0^{+20}_{-14}
ALESS073.1[h]	4.780	$10.64^{+0.05}_{-0.22}$	$794.33^{+790.56}_{-447.59}$	$8.97^{+0.34}_{-0.32}$	46.0^{+17}_{-14}
ALESS055.2[h]	4.680	$10.42^{+0.22}_{-0.55}$	$229.10^{+462.73}_{-168.84}$	$8.61^{+0.56}_{-0.42}$	44.0^{+18}_{-16}
ALESS069.3[h]	4.680	$10.36^{+0.22}_{-0.55}$	$194.98^{+421.61}_{-144.86}$	$8.55^{+0.56}_{-0.41}$	44.0^{+18}_{-16}
ALESS087.3[h]	4.680	$10.43^{+0.22}_{-0.54}$	$234.42^{+490.01}_{-169.86}$	$8.63^{+0.56}_{-0.42}$	44.0^{+18}_{-16}
ALESS099.1[h]	4.620	$10.36^{+0.23}_{-0.55}$	$199.53^{+417.07}_{-145.82}$	$8.55^{+0.56}_{-0.48}$	44.0^{+18}_{-16}
ALESS035.2[h]	4.570	$10.21^{+0.23}_{-0.55}$	$131.83^{+294.75}_{-99.47}$	$8.40^{+0.55}_{-0.42}$	43.0^{+19}_{-15}
ALESS103.3[h]	4.570	$10.21^{+0.22}_{-0.57}$	$131.83^{+304.69}_{-100.20}$	$8.40^{+0.56}_{-0.42}$	43.0^{+19}_{-15}
ALESS069.2[h]	4.380	$10.38^{+0.22}_{-0.52}$	$208.93^{+467.15}_{-152.69}$	$8.64^{+0.52}_{-0.44}$	43.0^{+18}_{-15}
ALESS088.2[h]	4.280	$10.64^{+0.14}_{-0.40}$	$151.36^{+285.16}_{-114.20}$	$8.58^{+0.53}_{-0.40}$	40.0^{+20}_{-13}
ALESS023.1[h]	4.070	$11.18^{+0.20}_{-0.54}$	$891.25^{+1150.49}_{-575.02}$	$8.90^{+0.35}_{-0.25}$	49.0^{+17}_{-15}
ALESS076.1[h]	3.970	$11.01^{+0.20}_{-0.49}$	$691.83^{+929.98}_{-451.95}$	$8.90^{+0.40}_{-0.25}$	44.0^{+17}_{-13}
ALESS037.2[h]	3.830	$10.55^{+0.10}_{-0.27}$	$213.80^{+562.45}$	$8.34^{+0.52}_{-0.47}$	47.0^{+19}_{-16}
ALESS002.2[h]	3.780	$11.00^{+0.19}_{-0.51}$	$588.84^{+996.05}_{-393.86}$	$8.64^{+0.35}_{-0.22}$	48.0^{+18}_{-14}
ALESS068.1[h]	3.780	$10.97^{+0.19}_{-0.57}$	$407.38^{+714.64}_{-287.15}$	$8.67^{+0.40}_{-0.34}$	47.0^{+17}_{-15}
MACSJ0032-arc[n]	3.631	7.89 ± 0.04	51^{+7}_{-10}	$5.49^{+0.14}_{-0.20}$	43.0 ± 5
ALESS110.5[h]	3.620	$10.55^{+0.16}_{-0.65}$	$151.36^{+451.20}_{-147.38}$	$8.61^{+0.55}_{-0.95}$	42.0^{+18}_{-16}
ALESS110.1[h]	3.580	$11.05^{+0.24}_{-0.51}$	$891.25^{+339.02}_{-401.47}$	$8.71^{+0.35}_{-0.26}$	66.0^{+1}_{-15}
ALESS116.1[h]	3.580	$10.92^{+0.17}_{-0.44}$	$549.54^{+652.72}_{-330.76}$	$8.52^{+0.17}_{-0.27}$	48.0^{+16}_{-12}
ALESS116.2[h]	3.580	$11.19^{+0.16}_{-0.50}$	$467.73^{+423.52}_{-293.96}$; –	$8.60^{+0.30}_{-0.16}$	44.0^{+16}_{-10}

by our simulated sample: $8.0 \leq \log(M_\star/M_\odot) \leq 11.0$. All the galaxies have a spectroscopically confirmed redshift, by a detection of either the Lyman-α line or some metal lines (e.g. [C II] or [O III]), while data taken from the ALMA Survey of Submillimeter Galaxies in the Extended Chandra Deep Field South (ALESS; da Cunha et al. 2015) have photometric redshifts, constrained by a subsample of spectroscopic observations (see the original references for more details).

At $z > 6.5$, our galaxy sample comprises single observations of normal star-forming galaxies with SFR $\leq 50\ M_\odot\ yr^{-1}$ with the only exception of B14-65666, which has an inferred SFR of $\approx 200\ M_\odot\ yr^{-1}$. We also mix normal star-forming galaxies of Capak et al. (2015), having SFR $\in [23.5, 64.7]\ M_\odot\ yr^{-1}$, with the sample of the ALESS, where star formation rates range from SFR $\geq 100\ M_\odot\ yr^{-1}$ up to SFR $\approx 1400\ M_\odot\ yr^{-1}$ (i.e. see the ALESS061.1 galaxy at $z = 6$).

At $z \lesssim 6$, galaxies with SFR $\geq 100\ M_\odot\ yr^{-1}$ have $\log(M_\star/M_\odot) > 10.25$ and their dust masses are typically one order of magnitude larger than the values of normal star-forming galaxies. It should be noted, on the other hand, that even when a direct detection of the continuum flux is available, the inferred values of M_d depend on the adopted dust temperature T_d and emissivity.[11] The case of MACS0416_Y1 provides a good example of a spectroscopically confirmed galaxy at $z \approx 8.3$ with a direct detection of the continuum flux, but the estimated dust mass varies by a factor of 2.2 when the assumed dust temperature differs by $\Delta T_d \approx 10$ K. Whenever the dust continuum emission is not detected, the table reports upper limits on M_d for the samples in Maiolino et al. (2015) and Capak et al. (2015); these are derived from relations introduced in Schaerer et al. (2015) and complemented by the computations in Mancini et al. (2015, 2016). Also in this case, we emphasize the tight dependence of these upper limits on the assumed grain temperatures $T_d \in [25, 45]$ K.

5 RESULTS

In this section, we discuss the results of our reference simulation (RefRun), which accounts for the full set of physical processes implemented in DUSTYGADGET. The corresponding set of physical parameters is listed in Table B1. As a comparison, we also explore a case where we do not consider grain growth in the ISM; i.e. we assume $\tau_{gg,0}^{-1} = 0$. We refer to this run as 'ProdOnly', to indicate that dust is produced only by stellar sources.

Section 5.1 shows the redshift evolution of the cosmic density parameter Ω_d, while Section 5.2 focuses on statistical properties of the dusty galaxy sample found in the RefRun: the dust mass function (DMF; Section 5.2.1), the dust-to-stellar mass relation (Section 5.2.2), and finally the dust-to-gas and dust-to-metal ratios (Section 5.2.3). A qualitative analysis of the dusty environment of a massive representative halo found at $z \approx 4$ is finally provided in Section 5.3.

5.1 Cosmic dust density parameter

Here, we investigate the redshift evolution of the cosmic dust density parameter Ω_d in the redshift range $4 \leq z \leq 10$. $\Omega_d(z)$ is defined as $\Omega_d(z) \equiv \rho_d(z)/\rho_{c,0}$, where $\rho_d(z)$ is the density of cosmic dust in the
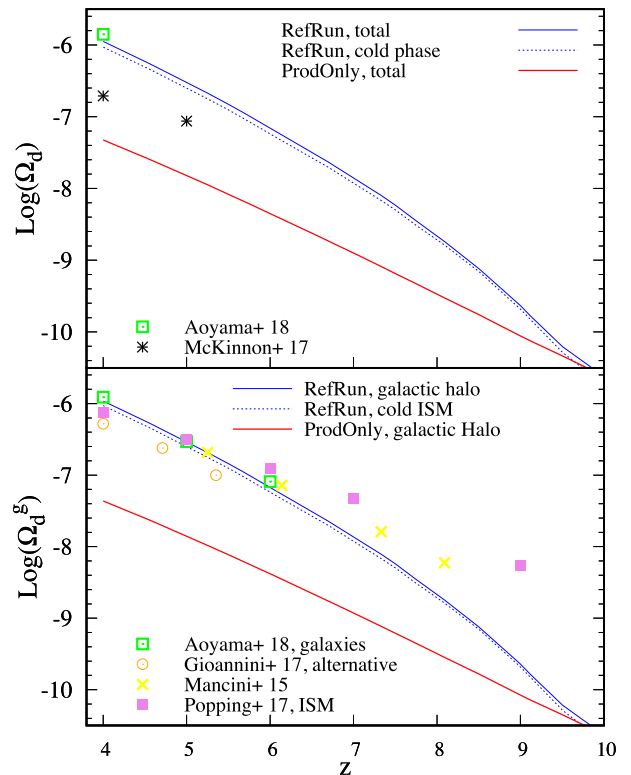
Figure 1. Top panel: Logarithm of $\Omega_d(z) \equiv \rho_d(z)/\rho_{c,0}$ as a function of redshift z; $\rho_{c,0} = 2.775 \times 10^{11}\ h^2\ M_\odot\ Mpc^{-3}$. The solid blue line refers to $\log(\Omega_d)$ computed from the reference run including both dust production and evolution (RefRun, total), while the blue dashed line shows values deriving from the cold phase environment in RefRun. $\log(\Omega_d)$, computed from a run in which dust is produced only by stellar sources (ProdOnly, total), is shown as solid red line. Black asterisks are values extrapolated from McKinnon et al. (2017) (see their fig. 4), while green squares refer to Aoyama et al. (2018, fig. 4). Bottom panel: Same as in the top panel but evaluated from the dust mass contained in galactic haloes [$\Omega_d^g(z)$]; here, the dashed blue line refers the cold ISM of the haloes. Green empty squares show data taken from Aoyama et al. (2018, fig. 5, top panel), violet filled squares are taken from Popping et al. (2017, fig. 10, 'fiducial' run), gold empty circles show the 'alternative scenario' in fig. 6 of Gioannini et al. (2017b), and finally, gold crosses refer to data in Mancini et al. (2015).

cosmological volume and $\rho_{c,0}$ is the critical density of the universe at $z = 0$.[12]

The top panel of Fig. 1 shows $\Omega_d(z)$ computed in the RefRun (solid blue line) and in the ProdOnly simulations (solid red line). The dotted blue line shows the same quantity evaluated from the dust mass in the cold phase of the RefRun. Green empty squares and black asterisks are values at $z \geq 4$ taken from Aoyama et al. (2018) and McKinnon et al. (2017), respectively.

In the redshift interval $10 \leq z \leq 15$ (not shown in the figure), the blue and red lines overlap, indicating that the dust mass is mainly produced by stellar sources (Pop III and Pop II stars). An accurate modelling of their stellar yields in this redshift range is required in order to make reliable predictions of the dust mass present in the first galaxies. Yet, an extensive investigation of these early phases of metal and dust enrichment would require a higher mass resolution. To investigate the impact of our set-up, we performed convergence

---

[11]Here, we point out that the dependence $M_d(T_d)$ applies to masses inferred in observations, while the dust mass computed in our simulation does not require any assumptions on its temperature.

[12]In accordance with the WMAP7 cosmology adopted in our simulation, the cosmic critical density at $z = 0$ is $\rho_{c,0} \approx 2.775 \times 10^{11}\ M_\odot\ h^2\ cMpc^{-3}$.

tests by running three identical hydrodynamical simulations increasing only the number of particles, up to 480^3. We found that a convergence between the different runs is obtained at $z \leq 9$. This implies that the dust content of the more massive and evolved galaxies investigated in this paper is not significantly affected by the adopted particle mass.

The increasing difference between the blue and red lines below $z \approx 9$ highlights the importance of grain growth in the ISM of the most massive and metal-enriched galaxies (Mancini et al. 2015), which leads to a cosmic dust density parameter at $z = 4$ that is more than one order of magnitude larger than in the ProdOnly case. The predictions of our reference run are very close to the ones of Aoyama et al. (2018) (a similar, GADGET-based implementation), while significantly differing from the values computed by McKinnon et al. (2017). This is mainly due to the $\tau_{\mathrm{gg},0}$ adopted in their simulation (see Table B1). Finally, a comparison between solid and dashed blue lines shows that the largest mass of dust is associated with the cold phase of the ISM, as also found by Aoyama et al. (2018) (see their fig. 4).

The bottom panel shows the evolution of the cosmic dust parameter considering only the dust mass confined in collapsed structures, $\Omega_{\mathrm{d}}^{\mathrm{g}}(z)$ (i.e. we consider the total mass of dust present in particles belonging to galactic DM haloes). As expected, the trend is very similar to the one presented in the top panel, since dust is produced by stars and it grows in the galactic ISM. When compared to other studies, our results show a remarkable agreement with the predictions of Aoyama et al. (2018) (green empty squares) and with semi-analytical/seminumerical models at $z \leq 6$. At higher z, some differences appear. The seminumerical model of Mancini et al. (2015) seems to overproduce dust, probably as a result of the more efficient grain growth parametrization adopted, where the grain growth time-scale is only modulated by the metallicity of the ISM and it is not sensitive to the cold gas density.

The comparison with the results of Popping et al. (2017) is complicated by the intrinsic differences among the models. In fact, while their 'fiducial' case is the closest to our RefRun in terms of adopted efficiency parameters, it runs on top of a halo catalogue generated with an extended Press–Schechter formalism, which converges with predictions of DM-only simulations only on scales larger than 30 h^{-1} cMpc. More importantly, in their model, grain growth is assumed to occur in molecular clouds, whose number density is inferred from the star formation law (Popping et al. 2017). In DUSTYGADGET, dust grains grow in the cold neutral medium, with a number density inferred from the physical conditions in the ISM (see Appendix A).

5.2 Statistics of dusty galaxies

This section investigates the redshift evolution of statistical properties and scaling relations of the simulated sample of dusty galaxies. The redshift evolution of the DMF is discussed in Section 5.2.1, the relation between stellar mass and dust mass in Section 5.2.2, and finally the dust-to-gas and dust-to-metal ratios in Section 5.2.3.

For an easier comparison with observed values, hereafter all the quantities are physical and converted from GADGET internal units.

5.2.1 Dust mass function

The DMF (ϕ) quantifies how galaxies are distributed in dust mass, in the cosmic volume. Fig. 2 shows the DMF[13] of our simulation at
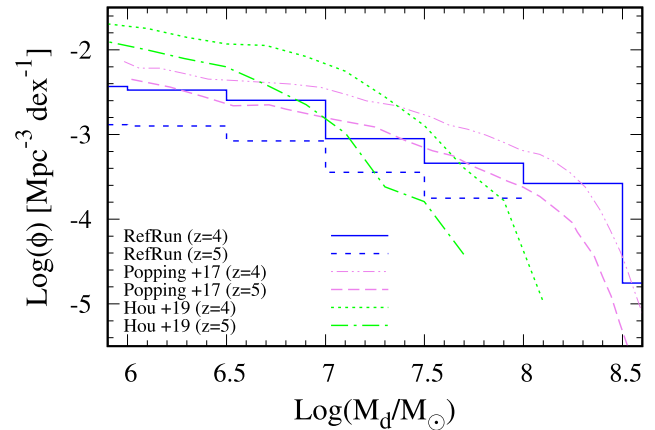

Figure 2. Logarithm of the DMF ϕ of the RefRun as a function of $\log(M_{\mathrm{d}}/M_{\odot})$ at $z \approx 4$ (solid blue line) and $z \approx 5$ (dashed blue line). The mass functions at similar redshifts from Popping et al. (2017) (violet dash–double-dotted/long-dashed lines) and Hou et al. (2019), based on the Aoyama et al. (2018) simulation (green dotted/dash–dotted lines), are also shown for a direct comparison.

redshifts $z = 5$ (dashed blue line) and $z = 4$ (solid blue line). As expected, the number of galaxies in each dust mass bin grows with time and galaxies progressively populate larger dust mass intervals.

Our predictions are compared with the results of Hou et al. (2019)[14] (green lines) and Popping et al. (2017) (violet lines). Despite the agreement found in the cosmic dust density parameter (see Fig. 1), the amplitude and slope of the DMF show significant variations across models. Compared to Hou et al. (2019), we find a flatter DMF, with fewer galaxies in the low-mass bins and more galaxies in the high dust mass intervals. Our slopes are closer to the ones found by Popping et al. (2017), but we find a smaller amplitude, probably as a result of less efficient grain growth in galaxies with low stellar mass (see discussion in Section 5.2.2). The differences with Hou et al. (2019) are likely due to a combination of different simulation volumes/resolution[15] and subgrid prescriptions for grain growth. In fact, the adopted rate has a similar functional form, but it is implemented in a different ISM phase. In DUSTYGADGET, grain growth occurs only in star-forming particles, when their number density exceeds a threshold of 132 h^{-2} cm^{-3}. In addition, its time-scale is modulated with the gas metallicity and the number density of star-forming particles, having a certain x_{c}; this implies that only when a galaxy has reached a considerable cold phase in star-forming regions, the dust can efficiently increase in mass. In Aoyama et al. (2018), grain growth occurs in dense gas particles, classified as particles with $n > 10$ cm^{-3}, with a time-scale that is modulated only by the gas metallicity and that corresponds to $\tau_{\mathrm{gg},0}(n_{\mathrm{c}}, T_{\mathrm{c}}) = 1.2 \, \mathrm{Myr}$.[16] The selection of these regions likely favours the evolution of a larger sample of dusty dwarfs, and disfavours objects with dust masses higher than $M_{\mathrm{d}} \sim 10^{7.5}$ M$_{\odot}$.

---

[13]The mass function ϕ is computed with a 0.5 bin size in $\log(M_{\mathrm{d}}/M_{\odot})$ scale.
[14]The analysis of Hou et al. (2019) is based on the simulation of Aoyama et al. (2018).
[15]The DMFs computed by Hou et al. (2019) are based on simulations with 50 h^{-1} Mpc^3 and 512^3 particles; hence, they simulate a larger volume but have less resolution compared to our RefRun (their DM and gas particle masses are 6.98×10^7 and 1.28×10^7 h^{-1} M$_{\odot}$, respectively).
[16]This value is obtained by rescaling n_{c} in τ_{gg} to 1000 cm^{-3} instead of 100, as in the original paper.
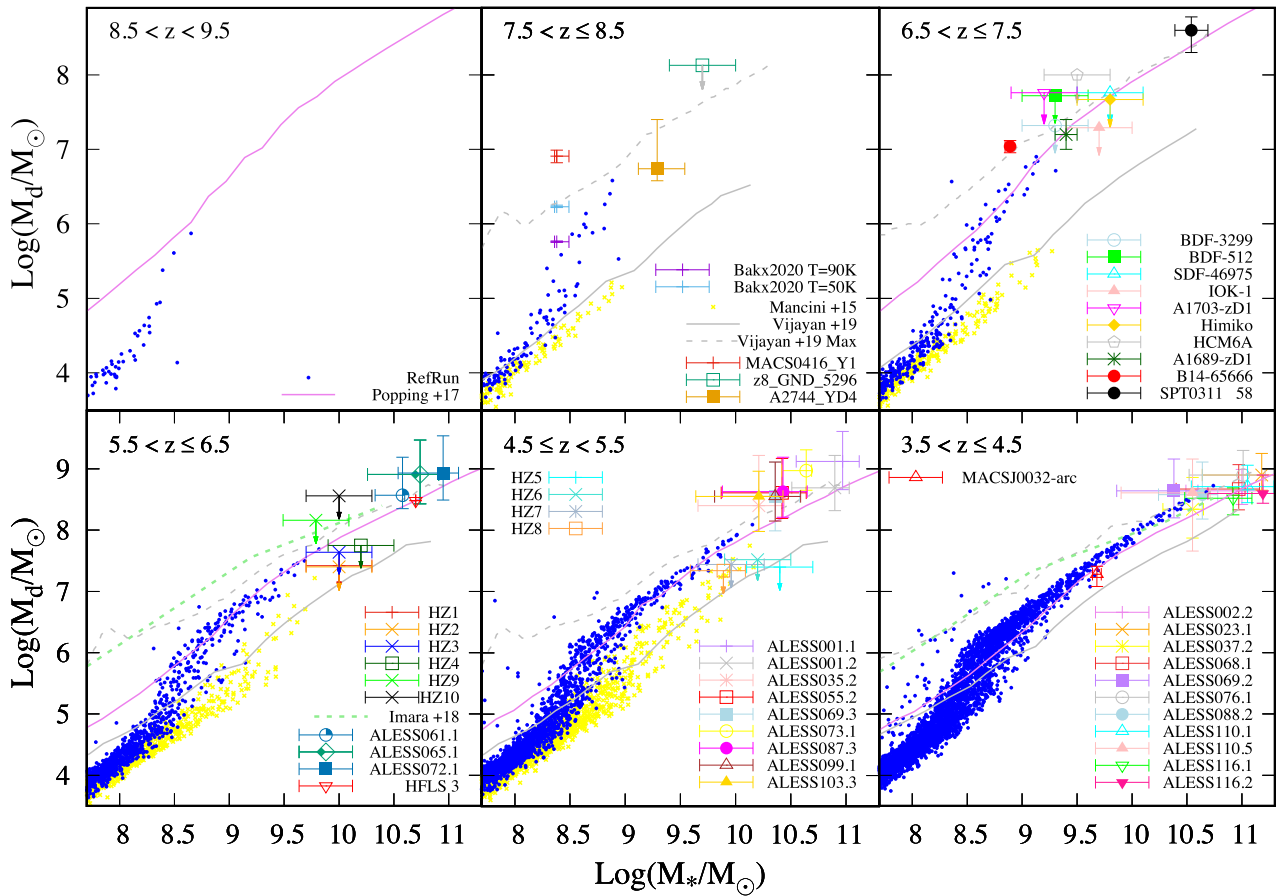
Figure 3. Logarithm of the dust mass M_d ($M_\odot$) as a function of the stellar mass $M_\star$ ($M_\odot$) for the galaxy sample with $\log(M_\star/M_\odot) > 7.5$. The redshift evolution of the galaxies is shown from $z \approx 9$ (top left) down to $z \approx 4$ (bottom right). In all panels, blue points are galaxies found in the reference run (RefRun), while the same objects predicted by the seminumerical model of Mancini et al. (2015) are shown as yellow points. When available, we also show the results of independent studies: the average trends computed by Popping et al. (2017) are shown as solid violet lines, grey solid and dashed lines are the fiducial/max models by Vijayan et al. (2019), and dashed green lines are the predictions by Imara et al. (2018). The observed dust and stellar masses can be found in Table 2.

5.2.2 Dust-to-stellar mass

Here, we explore how dust and stellar mass correlate in the galactic sample of the RefRun as a function of redshift, i.e. the relation $M_d(M_\star(z))$. Fig. 3 shows this evolution in different panels from $z = 9$ (top left) to $z = 4$ (bottom right), by selecting objects with $M_\star > 10^{7.5}$ $M_\odot$ (solid blue points, because smaller galaxies are poorly resolved given the currently adopted mass resolution. The data reported in Table 2 and in the figure show that current targets of ALMA observations have masses $M_\star \geq 10^{8.5}$ $M_\odot$. Each z in this figure is the middle value of a redshift interval $\Delta z = 1$, in which the observed sample of Table 2 is also grouped, for a better comparison.[17] Yellow crosses refer to the seminumerical model by Mancini et al. (2015, 2016), where galaxies are identified using the AMIGA halo finder and have the same stellar masses and metallicity as in the present DUSTYGADGET simulation.

At all redshifts, dust enrichment at the lowest mass end is dominated by stellar sources, consistent with the findings of Mancini et al. (2015, 2016). As expected, in this regime the dust mass grows linearly with the stellar mass, as a result of the equilibrium between dust formation by SNe and AGB stars and dust destruction by SN

shocks. As larger mass galaxies assemble, their cold ISM phase is more favourable to grain growth and the dust mass increases rapidly with stellar mass, reaching a saturation when accretion is limited by dust destruction and by the gas-phase metallicity. These features are particularly clear at $z \leq 6$ and are very consistent with the masses indicated by the ALESS sample and with what is observed locally in samples of galaxies spanning a sufficiently large range of metallicity (Asano et al. 2013a; de Bennassuti et al. 2014; Rémy-Ruyer et al. 2014; Zhukovska 2014; Ginolfi et al. 2018). Also note the excellent agreement with MACSJ0032-arc, a smaller object with SFR ≈ 50 $M_\odot$ yr^{-1} observed at $z \approx 3.6$.

At $z > 6$, most of the simulated galaxies have low $M_\star$, but there is a clear trend of increasing M_d in the most massive galaxies at each redshift, above the simple extrapolation of the linear regime. This is very interesting as it shows that, provided the right conditions are met, grain growth can operate even in relatively chemically unevolved galaxies. At these high redshifts, the major driver is likely to be the mass and density of the cold gas phase: indeed, the results of DUSTYGADGET always lie above the predictions of Mancini et al. (2015) where no density modulation of the grain growth time-scale was considered.

The dust masses in our largest simulated galaxies are consistent with the observationally inferred values at all redshifts, although at $z > 5$ the statistics at the high-mass end is poor, due to a combination

---

[17]Note that when more than one value of M_d for a single object is present in the table, we only show $M_d(T_d \approx 35$ K).

of two effects: (i) the relatively small simulated volume and (ii) a lack in mass resolution, which result in an artificial underestimation of star formation at high redshift, as discussed by Aoyama et al. (2019). Hence, a direct comparison with the data is not possible in some redshift bins. An example is provided by the $7.5 \leq z < 8.5$ bin (top middle panel). None of our galaxies has reached the right stellar mass to allow a direct comparison with A2744_YD4, although the trend of the most massive objects in our sample seems to be in line with its M_d. In addition, we point out that the observationally inferred dust masses are significantly affected by the adopted dust temperature and emissivity properties. As an example, in the top middle panel we report the dust mass estimated for the $z = 8.3$ galaxy MACS0416_Y1 by Tamura et al. (2019) and the recently revised values reported by Bakx et al. (2020) who provide a dust mass range that is remarkably close to our predicted values at comparable redshifts and stellar masses.

Interestingly, the simulated galaxies in the redshift range $6.5 \leq z < 7.5$ easily match the upper limits on M_d inferred for normal star-forming galaxies[18] but – at the same time – they are also consistent with the dust mass inferred for A1689-zD1. Hence, our environment-dependent dust enrichment naturally accounts for the variety of objects that have been observed at these high redshifts, some of which have a direct detection of their rest-frame IR continuum, while for others we can rely only on upper limits, even in very deep exposures. This is particularly encouraging, given that in previous studies the grain growth time-scale required to match these data had to be artificially reduced by one order of magnitude ($\tau_{gg,0} = 0.2$ Myr) and it was argued that the more efficient grain growth was due to a larger ISM density (Mancini et al. 2015).

Our data are also compared with average trends in the redshift interval $4 < z < 9$ predicted by the semi-analytical models of Popping et al. (2017) (solid violet line), Vijayan et al. (2019) (solid grey line for the fiducial case and dashed grey line for the maximum dust production efficiency case), and Imara et al. (2018) (dashed green line). In general, the agreement is very good at the high-mass end, where our simulated galaxies have already entered the regime where grain growth starts to be efficient. Conversely, at all z the semi-analytical models predict a larger dust mass at the low-mass end compared to DUSTYGADGET, probably due to differences in the adopted stellar dust yields or grain condensation efficiency.

5.2.3 Dust-to-metal and dust-to-gas ratios

In this section, we first study the average dust-to-metal ratio (DTM) of the galaxies found in the RefRun. This is defined as DTM $\equiv$ $M_d/M_{z,g}$, where M_d is the total mass of dust in each galaxy and $M_{z,g}$ is the total mass of metals in gas phase. Secondly, we focus our attention on the analogously defined dust-to-gas ratio $\mathcal{D}$. Both quantities are discussed as a function of the gas-phase metallicity Z_g, defined as total mass of gas-phase metals over total mass of gas ($Z_g = M_{z,g}/M_g$).[19] Fig. 4 shows the redshift evolution of $\log(DTM/0.44)$[20]

---

[18]In this redshift interval, none of the normal star-forming galaxies has a direct detection of the IR continuum from which the dust mass can be derived; the upper limits are then derived from Schaerer et al. (2015) by assuming $T_d = 35$ K.

[19]To show this quantity in solar units, we adopt the solar metallicity value $Z_\odot = 0.014$ (Asplund et al. 2009).

[20]For a better comparison with data from other models, the DTM ratio is normalized with respect to its value in the Milky Way, $DTM_{MW} = 0.44$, adopted in Popping et al. (2017).

in the top panels and $\log \mathcal{D}$ in the bottom panels. To facilitate a direct comparison with Fig. 3, the data points refer to a stellar mass range $8.0 \leq \log(M_\star/M_\odot) \leq 11.0$. Galaxies are also grouped in bins of stellar mass and shown with different symbols and colours (see the legend in the top panels). In the bottom right panel ($z \approx 4$), we also show $\log \mathcal{D}$ of the 'ProdOnly' simulation, with identical symbols but in grey-to-black colour gradient. Data from Vijayan et al. (2019) (ref/max case) are shown as coloured lines with the usual graphic style. Values based on observations available from Wiseman et al. (2017) at $z = 4.5$ are finally shown as black triangles.

Our points highlight a clear metallicity evolution in redshift from $z = 6$ to $z = 4$ following the assembly of larger mass galaxies (see the progression in the coloured points from blue to red and magenta). The DTM and $\mathcal{D}$ show a similar behaviour, quickly rising with Z_g at all z. The interpretation of these trends follows from the discussion of Fig. 3 and the mass–metallicity relation. Indeed, at low Z_g (low stellar masses), the dust content in galaxies is set by the balance between dust production by stellar sources and dust destruction. As Z_g increases, grain growth starts to be efficient, leading to a rapid increase in both DTM and $\mathcal{D}$. Finally, above $\log(Z_g/Z_\odot) \approx -1.5$, the dust content reaches an equilibrium controlled by grain growth and dust destruction. As a consequence, $\mathcal{D}$ becomes linearly proportional to the metallicity and DTM reaches a saturation, which persists across redshifts up to the highest metallicity [$\log(Z_g/Z_\odot) \approx -0.5$, i.e. ≈ 0.3 $Z_\odot$]. Interestingly, the DTM values of the simulated galaxies appear to be in very good agreement with the few available observations at $z = 5$ and $z = 4$ (Wiseman et al. 2017). First, the two data points at $z = 5$ (top middle panel) confirm that a significant increase in DTM can be observed in galaxies with a moderate difference in Z_g. Secondly, at $z \approx 4$ where more data are available (top right panel), observations are very well reproduced by DUSTYGADGET.

A large discrepancy across models appears in the top panels. While the DTM and $\mathcal{D}$ of Popping et al. (2017) follow the same general trends predicted by DUSTYGADGET, a rapid increase in their values occurs at high gas metallicity. At low metallicity (low stellar masses), their predicted $\mathcal{D}$ values are very consistent with our results. Since Fig. 3 shows larger dust masses for galaxies with $\log(M_\star/M_\odot) < 8.5$, we conclude that some of the differences may be due to a gas content in objects predicted by Popping et al. (2017) larger than the one in our simulated systems.

5.3 The dusty environment of a massive halo at $z \approx 4$

Thanks to its full hydrodynamical approach, DUSTYGADGET is also capable of providing accurate information on the distribution of dust within and around galaxies. This information can be compared with resolved observations and it is of great importance as it affects both luminosity and colours of observed galaxies.

With this aim in mind, here we qualitatively investigate the environment of one massive halo, DM0, with a total DM mass of $M_{DM} \approx 1.2 \times 10^{12}$ M$_\odot$ and a virial radius of $R_{vir} \approx 250$ kpc at $z \approx 4$, for which our present simulation is able to achieve an adequate spatial resolution.[21] The halo contains a central galaxy (G0) with gas mass $M_{gas} = 1.0 \times 10^{11}$ M$_\odot$, stellar mass $M_\star = 2.4 \times 10^{10}$ M$_\odot$, and dust mass $M_d = 1.62 \times 10^8$ M$_\odot$, producing stars at a rate of SFR ≈ 32 M$_\odot$ yr^{-1}. These properties are intermediate between

---

[21]The halo is composed of 14 249 DM particles, 12 834 gas particles, and 8580 stellar particles. It was selected among the most massive ones found at $z \approx 4$ not having a major merger event.
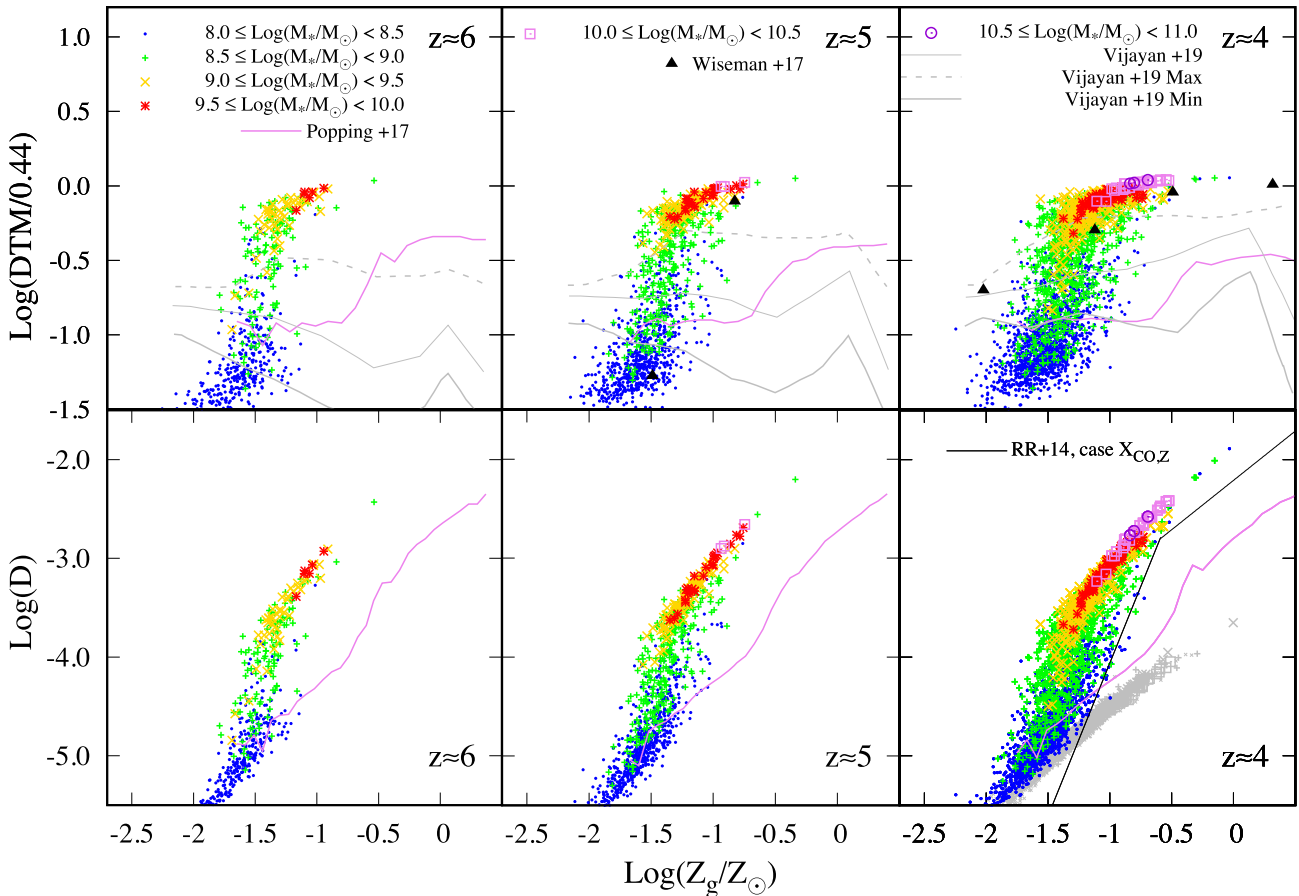
Figure 4. Redshift evolution of log(DTM/0.44) (top panels) and log $\mathcal{D}$ (bottom panels) as a function of log($Z_g/Z_\odot$), where Z_g is the gas-phase metallicity in solar units (see text for more details). The points refer to the RefRun and show galaxies in the stellar mass range $8 \leq \log(M_\star/M_\odot) \leq 11$, grouped in bins of one order of magnitude and shown with different symbols and colours (see the legend in the top left panel). For comparison, we also show the predictions of Popping et al. (2017) (solid violet line) and Vijayan et al. (2019) (solid grey line for the fiducial case and dashed grey line for the maximum dust production efficiency case); the triangles show data from Wiseman et al. (2017). Finally, in the bottom right panel ($z \approx 4$) we also show log $\mathcal{D}$ derived from the sample of the 'ProdOnly' simulation, with identical symbols but grey colours and the fit in Rémy-Ruyer et al. (2014) (solid black line for the broken power-law case, $X_{CO,Z}$), valid for a galactic sample at $z = 0$.

those observed for MACSJ0032-arc and for the lowest star-forming galaxies of the ALESS sample (e.g. ALESS088.2 or ALESS110.5). While a closer comparison with single objects is deferred to a future simulation with higher mass resolution, here we aim at describing a typical dusty environment found at the high end of our M_d–$M_\star$ relation at $z = 4$.

DM0 also contains 12 luminous satellites ($6 \leq \log(M_\star/M_\odot) \leq 8$) orbiting the central galaxy at a physical distance in the range $9 < d/\text{kpc} < 50$ and two dark satellites polluted by dust.

The dynamics of the gas present in the environment of G0 is shown in the left-hand panel of Fig. 5. In particular, we visualize its number density (n_{gas}) on a slice cut of a box centred on G0, and with a side length $L_b \approx 100$ kpc. To find the spatial distribution of the gas, the SPH particle distribution has been projected on to a Cartesian grid of 256 cells per side, corresponding to a spatial resolution of 0.39 kpc; $\log(n_{\text{gas}}/\text{cm}^{-3})$ is then shown as colour palette from red [$\log(n_{\text{gas}}/\text{cm}^{-3}) \approx -5.5$, typical of intergalactic environments] to blue [$\log(n_{\text{gas}}/\text{cm}^{-3}) \approx 1.6$, a galactic ISM density].

Despite the selection effect due to the geometric cut, some of the satellites are visible as blue, dense systems, often connected to the central object by cyan/green circumgalactic gas streams with $0.01 \text{ cm}^{-3} < n_{\text{gas}} \leq 0.2 \text{ cm}^{-3}$. Over a distance of $d \approx 50$ kpc, and

up to the box boundaries, the gas becomes more diffuse and its number density rapidly drops towards values closer the ones of the large scale, i.e. $n_{\text{gas}} < 10^{-4} \text{ cm}^{-3}$.

Finally, the velocity field of the gas, relative to the one of G0, is shown by blue vectors with length proportional to their module.[22] For the sake of clarity, the vectors are shown in representative subregions and only if their absolute value is $|\vec{v}| > 40 \text{ km s}^{-1}$. Large-scale motions are present almost everywhere in the box, with a complex pattern connecting the central galaxy with its surroundings.

To better resolve the dusty environment of G0, we further zoom in a smaller, central volume of side length $L_{b,c} \approx 37$ kpc covered by a new grid of 256 cells per side on which the original gas particles are projected. The resulting spatial resolution of the central region (indicated as a dashed square in the left-hand panel) is $d_c \approx 0.144$ kpc and its gas distribution is shown in the right-hand panel of Fig. 5.

---

[22]As for the number density, the velocity field has been projected on the same grid by mass weighting the velocity of each particle belonging to a grid cell.
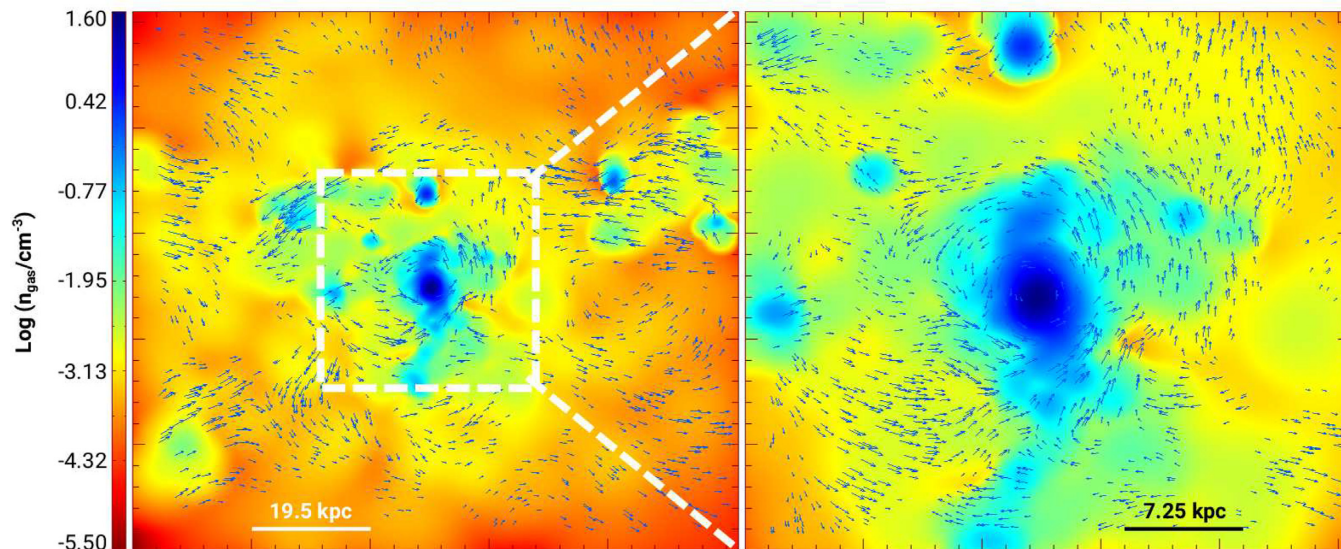
Figure 5. Gas distribution in the selected DM0 halo at $z \approx 4$. The gas number density n_{gas} (cm^{-3}) is mapped on a grid of 256^3 cells covering a cosmic volume of $L_b \approx 100$ kpc, physical, centred on the central galaxy (G0). The left-hand panel shows a slice cut of the volume containing the centre of G0, while the right-hand panel zooms into a central subregion of size ≈ 37 kpc. In both panels, the logarithmic value of n_{gas} is shown as colour palette from red (low density gas) to dark blue, while the velocity field of the gas is shown by blue arrows of different lengths spanning the velocity module interval 50–300 km s^{-1}.

The central, disc-like galaxy, G0, is better resolved on the scales presented in the right-hand panel and it shows a gas distribution that drops to $n_{gas} \approx 10^{-2}$ cm^{-3} within $r_{gas} \approx 12$ kpc (i.e. the green area). The central, dense area is quite compact and corresponds to the bulk of the star-forming ISM of the galaxy. It should be noted that while our mass resolution is not adequate to resolve the ISM clouds of the central region, it is sufficient to provide a first indication on how the cosmic dust spatially correlates with the distribution of the gas.

Fig. 6(a) shows the mass-weighted gas temperature on the same scales.[23]

The inner region of the galaxy ($d_{G0} \approx 2.5$ kpc) is dominated by warm gas with $T_{gas} \approx 10^3$ K (green–yellow areas[24]). T_{gas} progressively increases up to $T_{gas} \approx 10^4$ K in an intermediate region corresponding to the galaxy surroundings (light red areas here; cyan–green patterns in Fig. 5), while the outskirts of the halo are dominated by a low-density shocked gas (dark red here; green–yellow regions in Fig. 5) with temperatures as high as $T_{gas} \approx 3 \times 10^6$ K and densities lower than $n_{gas} < 10^{-3}$ cm^{-3}.

It is interesting to compare the above maps with the dust distribution predicted in the same region. This is shown in Fig. 6(b),

---

[23]Note that this is the DUSTYGADGET temperature of the SPH particles projected on the grid by weighting for their mass. To avoid quantization effects due to the SPH particle mass resolution on the gas properties, the grid has been selected to ensure that many gas particles contribute to the mass-weighted value in each cell. The yellow regions shown in the figure, for example, are extremely hot/dense cells to which many particles belong to. Finally note that a kernel smoothing is also applied when the data are plotted. Radiative effects are not accounted for at this scale with sufficient detail as our SPH scheme only accounts for an extragalactic UV background field, tuned on the large scale. This is not appropriate/significant at the galactic scale where the contribution of each star-forming region should be accounted for. In a future work, we will investigate this point by adopting a better mass and spatial resolution and performing radiative transfer simulations accounting for dust as in Glatzle et al. (2019).

[24]Also compare with isocontours of the cold gas mass; see figure caption for more details.

where the logarithm of the dust density (ρ_d in g cm^{-3}) is presented with a colour palette from dark blue (negligible content) to dark red [$\log(\rho_d/\mathrm{g\,cm}^{-3}) = -24$]. Isocontours of $\log \mathcal{D}$ are superimposed on this picture as black lines of different line styles, ranging from $\log \mathcal{D} = -6.0$ (solid lines) to $\log \mathcal{D} = -2.4$ (dash–triple-dotted lines).

By comparing Figs 6(a) and (b), it appears that dust spatially correlates only with the cold gas, where it is injected in the ISM by stars and where grain growth can occur. As a result, the spatially resolved dust-to-gas ratio is $\mathcal{D} > 3 \times 10^{-2}$, slightly higher than the average value measured in the Milky Way; note that the average value in the halo is $\mathcal{D} > 1.62 \times 10^{-3}$. The spatial distribution of the cold phase (isocontour lines in Fig. 6a) is more regular and centrally concentrated than that of dust grains (isocontours in Fig. 6b), indicating that winds are at place in the inner, star-forming regions and cause an inhomogeneous enrichment of metals and dust. The dust density rapidly decreases in the outskirts of the galaxy creating a very diffuse and irregular pattern (yellow and green regions). This shows that dust is present everywhere in the halo and often pollutes filaments connecting the central galaxy with its surrounding satellites. Its density is, on the other hand, orders of magnitude lower than in G0 [$\log(\rho_d/\mathrm{g\,cm}^{-3}) = -30$] and the grains are extremely diluted in the intergalactic gas, with $D < 10^{-3}$.

Dust grains moving into regions with very high temperature can suffer efficient sputtering decreasing their mass. Indeed, their spatial distribution appears to be anticorrelated with the location of gas shocked regions (see green–blue areas in Fig. 6 at $T_{gas} > 10^5$ K).

6 CONCLUSIONS

In this paper, we investigated the formation and chemical evolution of a sample of dusty galaxies found in a cosmological volume of co-moving box size of 30 h^{-1} cMpc. The sample is simulated with DUSTYGADGET, an extension of the SPH GADGET code, capable of accounting for dust production and evolution. Dust production
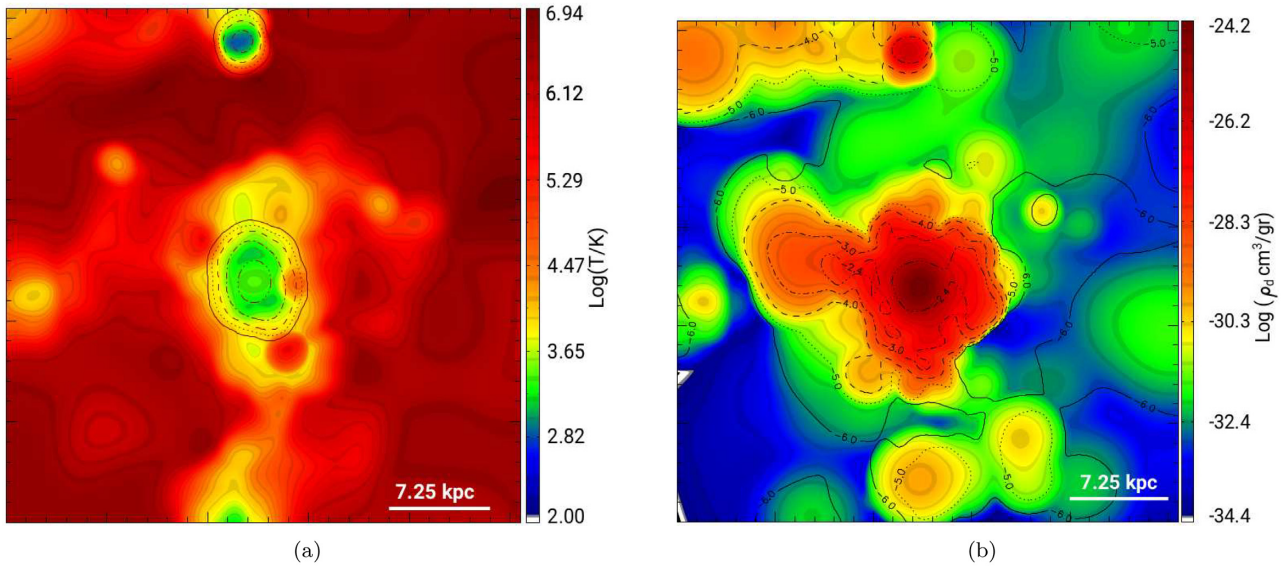
Figure 6. Gas temperature and dust density distributions in the same Cartesian grid and slice cut of the right-hand panel in Fig. 5 in a box of ≈37 kpc. (a) Logarithm of the gas temperature, $\log(T_{gas}/K)$, shown as a colour palette ranging from blue ($T_{gas} \approx 10^2$ K) to dark red ($T_{gas} > 10^6$ K). Values of the cold gas number density [$\log(n_c)$] are overplotted as black lines with different styles: $\log(n_c) = -4$ (solid), -2 (dotted), -1 (dashed), 0 (dash–dotted), and 1 (dash–triple-dotted). (b) Logarithm of the dust density, $\log(\rho_d/g\,cm^{-3})$, shown as a colour palette ranging from dark blue (negligible content) to dark red [$\log(\rho_d/g\,cm^{-3}) = -24$]. Values of the logarithm of the dust-to-gas ratio [$\log(\mathcal{D})$] are overplotted as black lines with different styles: $\log(\mathcal{D}) = -6$ (solid), -5 (dotted), -4 (dashed), -3 (dash–dotted), and -2.4 (dash–triple-dotted).

is modelled using mass- and metallicity-dependent stellar yields of AGB stars and SNe accounting for the effects of the RS. Dust grains are evolved in the galactic ISM, consistently with its hot and cold phases, through processes of destruction and grain growth by accretion of metals from the gas phase.

The simulated galaxy properties are compared with both independent theoretical predictions and observed samples of galaxies at $z \geq 4$. From this analysis, we find that the following:

(i) The evolution of the cosmic dust density parameter is driven by stellar dust production at $z \geq 10$. Accurate modelling of stellar dust yields, including those produced by metal-free and very metal-poor stars, is therefore very important in order to assess the mass, composition, and spatial distribution of interstellar dust in $z \approx 10$ systems. DUSTYGADGET is particularly suited for this purpose, as it follows metal and dust enrichment on stellar characteristic lifetimes, starting from a metallicity-dependent stellar IMF, and describing their chemical (AGB, SN, PISN) and mechanical (SN, PISN) feedback across a wide range of stellar masses. At $z < 10$, grain growth in the cold neutral phase of metal-enriched galaxies starts to be efficient, driving the evolution of Ω_d towards a value of $\approx 10^{-6}$ at $z = 4$, in good agreement with independent studies (Aoyama et al. 2018) and about an order of magnitude higher than predicted by stellar sources only.

(ii) In agreement with previous studies (Mancini et al. 2015, 2016), we find that, at any redshift, interstellar dust in low-mass galaxies, with $\log(M_\star/M_\odot) < 8.4$, is largely produced by AGBs and SNe, and the dust mass grows linearly with stellar mass. Across the mass range $8.5 < M_\star/M_\odot < 9.5$, the dust mass rapidly increases, with a wide dispersion, due to grain growth. We find that when the grain growth time-scale is computed consistently with the properties of the cold gas phase, the resulting dust mass at the high-mass end of the simulated galaxy distribution is in good agreement with the values inferred from either direct detections or deep upper limits of the rest-frame IR continuum in galaxies in the redshift range $4 \leq z$

< 8. This confirms previous indications of a density dependence of the grain growth time-scale, found in models (Mancini et al. 2015; Popping et al. 2017) and observations (Schneider, Hunt & Valiante 2016; Roman-Duval et al. 2017).

(iii) Although independent models show a fairly good agreement in predicting the evolution of the cosmic dust density parameter in the redshift range $4 < z < 6$, they differ in predicting the DMF at $z = 4$ and 5. This may be ascribed to differences in galaxy samples due to variations in simulation boxes/resolution, in intrinsic galaxy properties (particularly the mass fraction in cold gas), and in the subgrid implementation of grain growth. These differences are also reflected in the metallicity dependence of the dust-to-metal and dust-to-gas ratios, which greatly vary across models. It is encouraging that our simulated galaxies at $z = 5$ and 4 appear to have dust-to-metal ratios consistent with the few available observations (Wiseman et al. 2017).

(iv) Despite the limited resolution achieved in our simulation, a qualitative investigation of the properties of the most massive halo at $z \approx 4$ shows a complex gas distribution, connecting the central most massive disc-like galaxy to its satellites through low-density filaments. Dust grains appear to spatially correlate with the cold gas. In the innermost 2.5 kpc around the central massive galaxy, the dust-to-gas ratio is $\mathcal{D} > 0.03$, larger than the average value found in the Milky Way. The grains clearly escape the galaxy through galactic winds, reaching physical distances of 30 kpc from the central object. An intricate pattern connecting the central galaxy with its dusty, inefficiently star-forming satellites is clearly shown by our maps.

Although more detailed comparison with individually detected objects is deferred to future investigations, our results suggest that – provided the right conditions are met – dust enrichment can proceed rapidly at high redshift, aided by star formation and grain growth in the gas-rich regions of the first galaxies.

ACKNOWLEDGEMENTS

REFERENCES

Aoyama S., Hou K.-C., Shimizu I., Hirashita H., Todoroki K., Choi J.-H., Nagamine K., 2017, MNRAS, 466, 105

Aoyama S., Hou K.-C., Hirashita H., Nagamine K., Shimizu I., 2018, MNRAS, 478, 4905

Aoyama S. et al., 2019, MNRAS, 484, 1852

Aravena M. et al., 2016, ApJ, 833, 71

Arrigoni M., Trager S. C., Somerville R. S., Gibson B. K., 2010, MNRAS, 402, 173

Asano R. S., Takeuchi T. T., Hirashita H., Inoue A. K., 2013a, Earth Planets Space, 65, 213

Asano R. S., Takeuchi T. T., Hirashita H., Nozawa T., 2013b, MNRAS, 432, 637

Asano R. S., Takeuchi T. T., Hirashita H., Nozawa T., 2014, MNRAS, 440, 134

Asplund M., Grevesse N., Sauval A. J., Scott P., 2009, ARA&A, 47, 481

Bakx T. J. L. C. et al., 2020, MNRAS, 493, 4294

Barkana R., Loeb A., 2001, Phys. Rep., 349, 125

Behrens C., Pallottini A., Ferrara A., Gallerani S., Vallini L., 2018, MNRAS, 477, 552

Bekki K., 2015a, MNRAS, 449, 1625

Bekki K., 2015b, ApJ, 799, 166

Bekki K., Tsujimoto T., 2014, MNRAS, 444, 3879

Bianchi S., Schneider R., 2007, MNRAS, 378, 973

Bocchio M., Marassi S., Schneider R., Bianchi S., Limongi M., Chieffi A., 2016, A&A, 587, A157

Bradač M. et al., 2017, ApJ, 836, L2

Capak P. L. et al., 2015, Nature, 522, 455

Carilli C. L., Walter F., 2013, ARA&A, 51, 105

Caselli P., Hartquist T. W., Havnes O., 1997, A&A, 322, 296

Casey C. M., Narayanan D., Cooray A., 2014, Phys. Rep., 541, 45

Ceccarelli C., Viti S., Balucani N., Taquet V., 2018, MNRAS, 476, 1371

Cecchi-Pestellini C., Cacciola A., Iatì M. A., Saija R., Borghese F., Denti P., Giusto A., Williams D. A., 2010, MNRAS, 408, 535

Ceverino D., Klessen R. S., Glover S. C. O., 2018, MNRAS, 480, 4842

Chiaki G., Wise J. H., 2019, MNRAS, 482, 3933

Chiaki G., Marassi S., Nozawa T., Yoshida N., Schneider R., Omukai K., Limongi M., Chieffi A., 2015, MNRAS, 446, 2659

Clayton G. C., Gordon K. D., Bianchi L. C., Massa D. L., Fitzpatrick E. L., Bohlin R. C., Wolff M. J., 2015, ApJ, 815, 14

Cooray A. et al., 2014, ApJ, 790, 40

Crinklaw G., Federman S. R., Joseph C. L., 1994, ApJ, 424, 748

Cullen F., McLure R. J., Khochfar S., Dunlop J. S., Dalla Vecchia C., 2017, MNRAS, 470, 3006

da Cunha E. et al., 2015, ApJ, 806, 110

de Bennassuti M., Schneider R., Valiante R., Salvadori S., 2014, MNRAS, 445, 3039

de Bennassuti M., Salvadori S., Schneider R., Valiante R., Omukai K., 2017, MNRAS, 465, 926

Dell'Agli F., García-Hernández D. A., Schneider R., Ventura P., La Franca F., Valiante R., Marini E., Di Criscienzo M., 2017, MNRAS, 467, 4431

Dell'Agli F., Valiante R., Kamath D., Ventura P., García-Hernández D. A., 2019, MNRAS, 486, 4738

Dessauges-Zavadsky M. et al., 2017, A&A, 605, A81

Di Criscienzo M. et al., 2013, MNRAS, 433, 313

Draine B. T., 1995, Ap&SS, 233, 111

Draine B. T., 2003, ARA&A, 41, 241

Draine B. T., 2011, Physics of the Interstellar and Intergalactic Medium. Princeton Univ. Press, Princeton, NJ

Draine B. T., Salpeter E. E., 1979a, ApJ, 231, 77

Draine B. T., Salpeter E. E., 1979b, ApJ, 231, 438

Dunlop J. S. et al., 2013, MNRAS, 432, 3520

Dwek E., 1998, ApJ, 501, 643

Dwek E., 2016, ApJ, 825, 136

Eide M. B., Graziani L., Ciardi B., Feng Y., Kakiichi K., Di Matteo T., 2018, MNRAS, 476, 1174

Faisst A. L. et al., 2017, ApJ, 847, 21

Ferrarotti A. S., Gail H.-P., 2006, A&A, 447, 553

Finlator K., Keating L., Oppenheimer B. D., Davé R., Zackrisson E., 2018, MNRAS, 480, 2628

Gill S. P. D., Knebe A., Gibson B. K., 2004, MNRAS, 351, 399

Ginolfi M., Graziani L., Schneider R., Marassi S., Valiante R., Dell'Agli F., Ventura P., Hunt L. K., 2018, MNRAS, 473, 4538

Ginolfi M. et al., 2020, A&A, 633, A90

Gioannini L., Matteucci F., Vladilo G., Calura F., 2017a, MNRAS, 464, 985

Gioannini L., Matteucci F., Calura F., 2017b, MNRAS, 471, 4615

Gjergo E., Granato G. L., Murante G., Ragone-Figueroa C., Tornatore L., Borgani S., 2018, MNRAS, 479, 2588

Glatzle M., Ciardi B., Graziani L., 2019, MNRAS, 482, 321

Gordon K. D., Clayton G. C., Misselt K. A., Landolt A. U., Wolff M. J., 2003, ApJ, 594, 279

Graziani L., Salvadori S., Schneider R., Kawata D., de Bennassuti M., Maselli A., 2015, MNRAS, 449, 3137

Graziani L., de Bennassuti M., Schneider R., Kawata D., Salvadori S., 2017, MNRAS, 469, 1101

Haardt F., Madau P., 1996, ApJ, 461, 20

Hashimoto T. et al., 2019, PASJ, 71, 71

Heger A., Woosley S. E., 2002, ApJ, 567, 532

Hirano S., Hosokawa T., Yoshida N., Umeda H., Omukai K., Chiaki G., Yorke H. W., 2014, ApJ, 781, 60

Hirano S., Hosokawa T., Yoshida N., Omukai K., Yorke H. W., 2015, MNRAS, 448, 568

Hirashita H., 2000, PASJ, 52, 585

Hirashita H., 2012, MNRAS, 422, 1263

Hirashita H., 2013, in Proc. Life Cycle of Dust in the Universe: Observations, Theory, and Laboratory Experiments (LCDU2013), Taipei, Taiwan, 18–22 November 2013, p. 27

Hirashita H., 2015, MNRAS, 447, 2937

Hirashita H., Ferrara A., Dayal P., Ouchi M., 2014, MNRAS, 443, 1704

Hopkins P. F., Lee H., 2016, MNRAS, 456, 4174

Hopkins P. F., Kereš D., Oñorbe J., Faucher-Giguère C.-A., Quataert E., Murray N., Bullock J. S., 2014, MNRAS, 445, 581

Hou K.-C., Hirashita H., Michałowski M. J., 2016, PASJ, 68, 94

Hou K.-C., Aoyama S., Hirashita H., Nagamine K., Shimizu I., 2019, MNRAS, 485, 1727

Imara N., Loeb A., Johnson B. D., Conroy C., Behroozi P., 2018, ApJ, 854, 36

Inoue A. K., 2011a, Earth Planets Space, 63, 1027

Inoue A. K., 2011b, MNRAS, 415, 2920

Inoue A. K. et al., 2016, Science, 352, 1559

Iye M. et al., 2006, Nature, 443, 186

Jones A. P., Tielens A. G. G. M., Hollenbach D. J., McKee C. F., 1994, ApJ, 433, 797

Jones A. P., Fanciullo L., Köhler M., Verstraete L., Guillet V., Bocchio M., Ysard N., 2013, A&A, 558, A62

Katz H. et al., 2019, MNRAS, 487, 5902

Khakhaleva-Li Z., Gnedin N. Y., 2016, ApJ, 820, 133

Kimm T., Cen R., 2013, ApJ, 776, 35

Knollmann S. R., Knebe A., 2009, ApJS, 182, 608

Knudsen K. K., Watson D., Frayer D., Christensen L., Gallazzi A., Michałowski M. J., Richard J., Zavala J., 2017, MNRAS, 466, 138

Komatsu E. et al., 2011, ApJS, 192, 18

Koprowski M. P., Dunlop J. S., Michałowski M. J., Coppin K. E. K., Geach J. E., McLure R. J., Scott D., van der Werf P. P., 2017, MNRAS, 471, 4155

Kuo T.-M., Hirashita H., 2012, MNRAS, 424, L34

Laporte N. et al., 2017, ApJ, 837, L21

Ma X. et al., 2018, MNRAS, 478, 1694

Ma X. et al., 2019, MNRAS, 487, 1844

McKee C., 1989, in Allamandola L. J., Tielens A. G. G. M., eds, Proc. IAU Symp. 135, Interstellar Dust. Kluwer, Dordrecht, p. 431

McKee C. F., Ostriker J. P., 1977, ApJ, 218, 148

McKinnon R., Torrey P., Vogelsberger M., Hayward C. C., Marinacci F., 2017, MNRAS, 468, 1505

McKinnon R., Vogelsberger M., Torrey P., Marinacci F., Kannan R., 2018, MNRAS, 478, 2851

Maio U., Dolag K., Ciardi B., Tornatore L., 2007, MNRAS, 379, 963

Maio U., Ciardi B., Yoshida N., Dolag K., Tornatore L., 2009, A&A, 503, 25

Maio U., Ciardi B., Dolag K., Tornatore L., Khochfar S., 2010, MNRAS, 407, 1003

Maio U., Petkova M., De Lucia G., Borgani S., 2016, MNRAS, 460, 3733

Maiolino R. et al., 2015, MNRAS, 452, 54

Mancini M., Schneider R., Graziani L., Valiante R., Dayal P., Maio U., Ciardi B., Hunt L. K., 2015, MNRAS, 451, L70

Mancini M., Schneider R., Graziani L., Valiante R., Dayal P., Maio U., Ciardi B., 2016, MNRAS, 462, 3130

Marassi S., Chiaki G., Schneider R., Limongi M., Omukai K., Nozawa T., Chieffi A., Yoshida N., 2014, ApJ, 794, 100

Marassi S., Schneider R., Limongi M., Chieffi A., Bocchio M., Bianchi S., 2015, MNRAS, 454, 4250

Marassi S., Schneider R., Limongi M., Chieffi A., Graziani L., Bianchi S., 2019, MNRAS, 484, 2587

Marrone D. P. et al., 2018, Nature, 553, 51

Micelotta E. R., Dwek E., Slavin J. D., 2016, A&A, 590, A65

Nanni A., Bressan A., Marigo P., Girardi L., 2013, MNRAS, 434, 2390

Nanni A., Bressan A., Marigo P., Girardi L., 2014, MNRAS, 438, 2328

Narayanan D., Davé R., Johnson B. D., Thompson R., Conroy C., Geach J., 2018, MNRAS, 474, 1718

Nozawa T., Kozasa T., Umeda H., Maeda K., Nomoto K., 2003, ApJ, 598, 785

Nozawa T., Kozasa T., Habe A., 2006, ApJ, 648, 435

Nozawa T., Kozasa T., Habe A., Dwek E., Umeda H., Tominaga N., Maeda K., Nomoto K., 2007, ApJ, 666, 955

Olsen K. P., Greve T. R., Narayanan D., Thompson R., Davé R., Rios L. N., Stawinski S., 2017, ApJ, 846, 105

Ono Y. et al., 2018, PASJ, 70, S10

Padovani P., Matteucci F., 1993, ApJ, 416, 26

Pallottini A., Ferrara A., Bovino S., Vallini L., Gallerani S., Maiolino R., Salvadori S., 2017, MNRAS, 471, 4128

Piovan L., Chiosi C., Merlin E., Grassi T., Tantalo R., Buonomo U., Cassarà L. P., 2011, preprint (arXiv:1107.4541)

Popping G., Somerville R. S., Galametz M., 2017, MNRAS, 471, 3152

Rémy-Ruyer A. et al., 2014, A&A, 563, A31

Roman-Duval J., Bot C., Chastenet J., Gordon K., 2017, ApJ, 841, 72

Romano D., Chiappini C., Matteucci F., Tosi M., 2005, A&A, 430, 491

Romano D., Karakas A. I., Tosi M., Matteucci F., 2010, A&A, 522, A32

Saitoh T. R., 2017, AJ, 153, 85

Sarangi A., Cherchneff I., 2015, A&A, 575, A95

Schaerer D., Boone F., Zamojski M., Staguhn J., Dessauges-Zavadsky M., Finkelstein S., Combes F., 2015, A&A, 574, A19

Schneider R., Ferrara A., Salvaterra R., 2004, MNRAS, 351, 1379

Schneider R., Omukai K., Bianchi S., Valiante R., 2012a, MNRAS, 419, 1566

Schneider R., Omukai K., Limongi M., Ferrara A., Salvaterra R., Chieffi A., Bianchi S., 2012b, MNRAS, 423, L60

Schneider R., Hunt L., Valiante R., 2016, MNRAS, 457, 1842

Seab C. G., 1987, in Hollenbach D. J., Thronson H. A. Jr, eds, Astrophysics and Space Science Library, Vol. 134, Interstellar Processes. Reidel, Dordrecht, p. 491

Silvia D. W., Smith B. D., Shull J. M., 2010, ApJ, 715, 1575

Silvia D. W., Smith B. D., Shull J. M., 2012, ApJ, 748, 12

Slavin J. D., Dwek E., Jones A. P., 2015, ApJ, 803, 7

Sluder A., Milosavljevic M., Montgomery M. H., 2018, MNRAS, 480, 5580

Smit R., Bouwens R. J., Labbé I., Franx M., Wilkins S. M., Oesch P. A., 2016, ApJ, 833, 254

Sofia U. J., Lauroesch J. T., Meyer D. M., Cartledge S. I. B., 2004, ApJ, 605, 272

Somerville R. S., Popping G., Trager S. C., 2015, MNRAS, 453, 4337

Springel V., 2005, MNRAS, 364, 1105

Springel V., Hernquist L., 2003, MNRAS, 339, 289

Springel V., White S. D. M., Tormen G., Kauffmann G., 2001, MNRAS, 328, 726

Strandet M. L. et al., 2017, ApJ, 842, L15

Sugahara Y., Ouchi M., Harikane Y., Bouché N., Mitchell P. D., Blaizot J., 2019, ApJ, 886, 29

Sutherland R. S., Dopita M. A., 1993, ApJS, 88, 253

Takahashi K., Yoshida T., Umeda H., 2018, ApJ, 857, 111

Tamura Y. et al., 2019, ApJ, 874, 27

Thielemann F.-K. et al., 2003, Nucl. Phys. A, 718, 139

Tielens A. G. G. M., McKee C. F., Seab C. G., Hollenbach D. J., 1994, ApJ, 431, 321

Tornatore L., Ferrara A., Schneider R., 2007a, MNRAS, 382, 945

Tornatore L., Borgani S., Dolag K., Matteucci F., 2007b, MNRAS, 382, 1050

Tsai J. C., Mathews W. G., 1995, ApJ, 448, 84

Valiante R., Schneider R., Bianchi S., Andersen A. C., 2009, MNRAS, 397, 1661

Valiante R., Schneider R., Salvadori S., Bianchi S., 2011, MNRAS, 416, 1916

Valiante R., Schneider R., Salvadori S., Gallerani S., 2014, MNRAS, 444, 2442

van den Hoek L. B., Groenewegen M. A. T., 1997, A&AS, 123, 305

Ventura P. et al., 2012a, MNRAS, 420, 1442

Ventura P. et al., 2012b, MNRAS, 424, 2345

Ventura P., Karakas A., Dell'Agli F., García-Hernández D. A., Guzman-Ramirez L., 2018, MNRAS, 475, 2282

Vijayan A. P., Clay S. J., Thomas P. A., Yates R. M., Wilkins S. M., Henriques B. M., 2019, MNRAS, 489, 4072

Vincenzo F., Matteucci F., Belfiore F., Maiolino R., 2016, MNRAS, 455, 4183

Vogelsberger M., Genel S., Sijacki D., Torrey P., Springel V., Hernquist L., 2013, MNRAS, 436, 3031

Watson D., Christensen L., Knudsen K. K., Richard J., Gallazzi A., Michałowski M. J., 2015, Nature, 519, 327

Weingartner J. C., 2004, in Witt A. N., Clayton G. C., Draine B. T., eds, ASP Conf. Ser. Vol. 309, Astrophysics of Dust. Astron. Soc. Pac., San Francisco, p. 453

Weingartner J. C., Draine B. T., 1999, ApJ, 517, 292

Weingartner J. C., Draine B. T., 2001, ApJS, 134, 263

Wiersma R. P. C., Schaye J., Smith B. D., 2009, MNRAS, 393, 99

Wilkins S. M., Bouwens R. J., Oesch P. A., Labbé I., Sargent M., Caruana J., Wardlow J., Clay S., 2016, MNRAS, 455, 659

Wise J. H., Turk M. J., Norman M. L., Abel T., 2012, ApJ, 745, 50

Wiseman P., Schady P., Bolmer J., Krühler T., Yates R. M., Greiner J., Fynbo J. P. U., 2017, A&A, 599, A24

Wolfire M. G., McKee C. F., Hollenbach D., Tielens A. G. G. M., 2003, ApJ, 587, 278

Wood K., Loeb A., 2000, ApJ, 545, 86

Woosley S. E., Weaver T. A., 1995, ApJS, 101, 181

Xu H., Wise J. H., Norman M. L., Ahn K., O'Shea B. W., 2016, ApJ, 833, 84

Yoshida N., Abel T., Hernquist L., Sugiyama N., 2003, ApJ, 592, 645

Zhukovska S., 2014, A&A, 562, A76

Zhukovska S., Gail H.-P., Trieloff M., 2008, A&A, 479, 453

Zhukovska S., Dobbs C., Jenkins E. B., Klessen R. S., 2016, ApJ, 831, 147

Zhukovska S., Henning T., Dobbs C., 2018, ApJ, 857, 94

Zu Y., Weinberg D. H., Davé R., Fardal M., Katz N., Kereš D., Oppenheimer B. D., 2011, MNRAS, 412, 1059

APPENDIX A: MULTIPHASE ISM MODEL

Springel & Hernquist (2003) implemented a subresolution model that uses spatially averaged physical properties to describe a two-phase ISM contained in each SPH gas particle. In their picture, the two phases (hot and cold gases)[25] survive in pressure equilibrium as prescribed by the equations introduced in McKee & Ostriker (1977).

Volume-averaged quantities, e.g. the gas density (ρ_g) and temperature (T_g), can be simply related to the average values of each phase, i.e. $\rho_g = \rho_h + \rho_c$. Similarly, the average thermal energy of the gas per unit volume can be written as $\epsilon_g = \rho_h u_h + \rho_c u_c$, where u_h and u_c are the energy per unit mass of the hot and cold components, respectively.

The cold phase represents condensed clouds where stars form and it is assumed at constant temperature $T_c \sim 10^3$ K (i.e. constant u_c), while the hot phase represents their ambient gas, shock heated by SN explosions. T_h evolves from $T_h > 10^6$ K down to $T_h \sim 10^4$ K by a molecule- and metallicity-dependent cooling function until the gas becomes neutral and flows into the cold phase. The two phases can then exchange mass and energy through three main feedback processes: formation of stellar mass in cold clouds, cloud evaporation induced by SN explosions, and cloud growth caused by thermal instabilities through cooling of the hot phase.

Star formation is modelled as a self-regulated, 'quiescent' process that converts cold clouds into stars on a characteristic time-scale $t_\star$. At each time-step dt, a mass fraction β of these stars is assumed to evolve by accounting for the assumed IMF and the mass-dependent lifetime of SN progenitors. As a result, the cold phase is depleted at a rate $\rho_c/t_\star$, while the hot phase increases due to gas (enriched with metals) returned by SN explosions by a term equal to $A\beta\rho_c/t_\star$, where A is an efficiency factor that quantifies cloud evaporation inside the hot bubbles of exploding SN.[26]

Cloud formation and growth (leading to a mass transfer from the ambient gas) are finally due to a thermal instability throughout radiative losses (see Springel & Hernquist 2003 and references therein). Thermal instability is assumed to occur only when the density is above a given threshold value, $\rho > \rho_{th}$,[27] and it is controlled by the parameter f. When $\rho > \rho_{th}$, $f = 0$ and the mechanism operates creating clouds, otherwise $f = 1$. Finally note that during their growth, the volumes of the cold and hot phases are assumed constant.

Under the previous assumptions, the evolution of the hot and cold phases throughout star formation, evolution, and mass exchange is then described by the following coupled equations:

$$\frac{d\rho_c}{dt} = -\frac{\rho_c}{t_\star} - A\beta\frac{\rho_c}{t_\star} + \frac{1-f}{u_h - u_c}\Lambda(\rho_h, u_h), \tag{A1}$$

$$\frac{d\rho_h}{dt} = \beta\frac{\rho_c}{t_\star} + A\beta\frac{\rho_c}{t_\star} - \frac{1-f}{u_h - u_c}\Lambda(\rho_h, u_h), \tag{A2}$$

where ϵ_{SN} is the IMF-averaged energy released by SNe per unit stellar mass formed. The evolution of the temperature of the hot component is given instead by the equation of energy conservation:

$$\frac{d}{dt}(\rho_h u_h + \rho_c u_c) = \beta\frac{\rho_c}{t_\star}u_{SN} - \Lambda(\rho_h, u_h) - (1-\beta)\frac{\rho_c}{t_\star}u_c, \tag{A3}$$

where the first term describes the heating rate arising from SNe, the second term accounts for the radiative losses of the hot phase, and the third term describes the loss of energy caused by the transformation of gas into stars, which are assumed to be at the temperature of the cold clouds. Note that in this self-regulated star formation, the value of u_h is determined only by the effects of star formation and feedback (see equations 8–10 in Springel & Hernquist 2003).

In the implementation of dust evolution, we often refer to the mass fraction of cold clouds x_c, defined as $x_c \equiv \rho_c/\rho$.

APPENDIX B: PROPERTIES OF MODELS WHERE DUST EVOLUTION HAS BEEN IMPLEMENTED

Here, we simply collect the efficiency parameters adopted by the theoretical models described in Section 4. Whenever the models adopt different scaling values of gas number density, temperature, and metallicity, they are aligned to the formulae in Section 2 to allow a direct comparison. Table B1 collects the above data and can be used to understand differences discussed in Section 5.

---

[25]In this paper, variables with a subscript 'c' refer to all the variables of the cold phase, while 'h' indicates the hot one.

[26]The factors A and the time-scale $t_\star$ are assumed to depend only on density as $A = A_0(\rho/\rho_{th})^{-4/5}$ and $t_\star = t_0^\star(\rho/\rho_{th})^{-1/2}$, where the parameters A_0 and $t_0^\star$ are set to 10^3 and 2.1 Gyr. See Springel & Hernquist (2003) for more details.

[27]In Section 3, we introduced the threshold value adopted in the simulation in terms of the number density of the gas, $n_{th} = \rho_{th}/(\mu m_H)$, where μ is the mean molecular weight of the gas and m_H is the mass of the hydrogen nucleus.

Table B1. Properties of semi-analytical, seminumerical, and numerical models where dust evolution has been implemented. The parameters assumed for the various dust processes are extracted from the original paper models and references therein (see Table 1). References in this table: (*a*) Springel & Hernquist (2003), Maio et al. (2010); (*b*) Somerville et al. (2015); (*d*) Aoyama et al. (2017); (*i*) Bianchi & Schneider (2007); (*h*) Piovan et al. (2011).

	Popping+17	Mancini+15	Gioannini+17	Aoyama+18	McKinnon+17	dustygadget
Cosmology	WMAP5	WMAP7	Planck 2016	Planck 2016	Planck 2014	WMAP7
L_b (cMpc h^{-1})	–	30	–	50	25	30
M_{DM} ($M_\odot\ h^{-1}$)	–	6×10^7	–	6.89×10^7	8.22×10^6	6×10^7
M_g ($M_\odot\ h^{-1}$)	–	9×10^6	–	1.28×10^7	1.53×10^6	9×10^6
ISM phases	diff/H_2 [b]	$x_c = 0.5$	x_c*	$f_{dense} = 0.1$ [d]	–	Hot/cold [a]
Dust sources	SNIa–II/AGB	SNII/AGB	SNII/AGB	SNIa–II/AGB	SNIa–II/AGB	PISN/SNII/AGB
RS in yields	Y (avg) [i]	Y (tbl) [i]	Y (avg) [h]	N	N	Y (tbl) [i]
Astration	Y	Y	Y	Y	Y	Y
$\tau_{gg,0}$ (Myr)	1.5	2.0	2.0	1.2	4	2.0
f_{SN}	0.36	0.15	1	–	1	0.15
ϵ_d	*	0.48	0.1	0.1	0.3	0.48
M_s ($M_\odot$)	600–980*	2040	1360	?	7412	2040
GS distribution	N	N	N	Y	N	N

This paper has been typeset from a TEX/LATEX file prepared by the author.